Remote Sensing of Environment 168 (2015) 219–238

Contents lists available at ScienceDirect

Remote Sensing of Environment

journal homepage: www.elsevier.com/locate/rse

Understanding the subsidence process of a quaternary plain by combining geological and hydrogeological modelling with satellite InSAR data: The Acque Albule Plain case study

Francesca Bozzano [a,b], Carlo Esposito [a], Stefania Franchi [a], Paolo Mazzanti [a,b,*], Daniele Perissin [c], Alfredo Rocca [a,b], Emanuele Romano [d]

[a] Earth Sciences Department of Sapienza University of Rome, p.le Aldo Moro 5, 00185 Rome, Italy
[b] NHAZCA S.r.l. Spin-off of Sapienza University of Rome, via Cori snc, 00177 Rome, Italy
[c] Lyle School of Civil Engineering, Purdue University, 550 Stadium Mall Drive West Lafayette, IN 47907, United States
[d] Water Research Institute — National Research Council, Via Salaria 29, 300, 00015, Monterotondo Scalo, Rome, Italy

ARTICLE INFO

Article history:
Received 1 November 2014
Received in revised form 27 June 2015
Accepted 9 July 2015
Available online 24 July 2015

Keywords:
Synthetic Aperture Radar Interferometry
Subsidence
Hydrogeological modelling
Mining
Dewatering
Compressible soil

ABSTRACT

This paper focuses on a multidisciplinary study carried out in an urban area affected by subsidence and related structural damages. The study area is located about 20 km east of Rome (Italy) and is characterised by relevant groundwater exploitation for various purposes as well as by the presence of compressible soils immediately below the ground level. Extensive processing at different scales of SAR satellite images (ERS and ENVISAT provided by ESA in the frame of a CAT-1 project) by means of A-DInSAR technique was performed. The time histories of ground displacements, have been analysed in combination with a detailed geological setting of the study area and with the hydrogeological changes occurred in the last decades (as the response to the anthropic stress) based on a large piezometric dataset. This comprehensive dataset allowed us to describe the space and time distributions of the subsidence process. The spatial pattern and deformation rate change is attributed to the following causes: i) the changes in the groundwater levels due to the intensification of mine exploitation (requiring dewatering operations) and ii) the distribution and thickness of recent compressible deposits. Specifically, it is derived that the groundwater level variations drive the timing of subsidence triggering over the area, whereas the local geological conditions control the magnitude of the deformation process.

1. Introduction

Ground subsidence is a common process occurring on the ground surface. Subsidence can be controlled by natural processes, such as volcanic activities (Lu, Masterlark, Power, Dzurisin, & Wicks, 2002), but quite often it can be triggered or accelerated by human activities.

Underground excavations (e.g., mining and tunnelling) and new settlements on the ground surface are likely the most common anthropogenic factors causing local scale subsidence (Guéguen et al., 2009; Jung, Kim, Jung, Min, & Won, 2007; Samsonov, d'Oreye, & Smets, 2013). However, fluid and gas exploitation are most commonly associated with regional scale subsidence involving square kilometre areas (Dixon et al., 2006; Meckel, ten Brink, & Williams, 2006; Teatini et al., 2011). Groundwater exploitation is likely the most challenging process as it generally affects large cities that require huge quantities of water for human activities. These processes have been extensively reported worldwide for several important cities, such México City (Cabral-Cano et al., 2008; Chaussard, Wdowinski, Cabral-Cano, & Amelung, 2014; Osmanoğlu, Dixon, Wdowinski, Cabral-Cano, & Jiang, 2011), Bangkok (Phien-wej, Giao, & Nutalaya, 2006), Shanghai, Tianjin, Beijing, China (Xue, Zhang, Ye, Wu, & Li, 2005), Lhokseumawe, Medan, Jakarta, Bandung, Blanakan, Pekalongan, Bungbulang, and Semarang, Indonesia (Chaussard, Amelung, Abidin, & Hong, 2013), Taipei, Taiwan (Hung et al., 2011), Florence (Colombo, Farina, Moretti, Nico, & Prati, 2003), Prato (Raucoules, Le Mouélic, Carnec, Maisons, & King, 2003), and Bologna (Modoni et al., 2013).

In some cases, subsidence can be on the order of some metres with velocities of some decimetres per year, thus quite often causing damage to buildings and infrastructures. In other cases, more minor displacements can be revealed only by instrumental analyses.

Among the ground displacement measurement techniques, satellite differential InSAR (Berardino, Fornaro, Lanari, & Sansosti, 2002; Bürgmann et al., 2000, Ferretti, Prati, & Rocca, 2000, 2001, Ferretti et al., 2011, 2000, 2001; Gabriel, Goldstein, & Zebker, 1989; Hooper, Zebker, Segall, & Kampes, 2004, Kampes, 2006; Massonnet, Briole, &

* Corresponding author at: Earth Sciences Department of Sapienza University of Rome, p.le Aldo Moro 5, 00185 Rome, Italy.
E-mail addresses: francesca.bozzano@uniroma1.it (F. Bozzano), carlo.esposito@uniroma1.it (C. Esposito), stefaniafranchi84@gmail.com (S. Franchi), paolo.mazzanti@nhazca.com (P. Mazzanti), perissin@purdue.edu (D. Perissin), alfredo.rocca@nhazca.com (A. Rocca), romano@irsa.cnr.it (E. Romano).

http://dx.doi.org/10.1016/j.rse.2015.07.010
0034-4257/

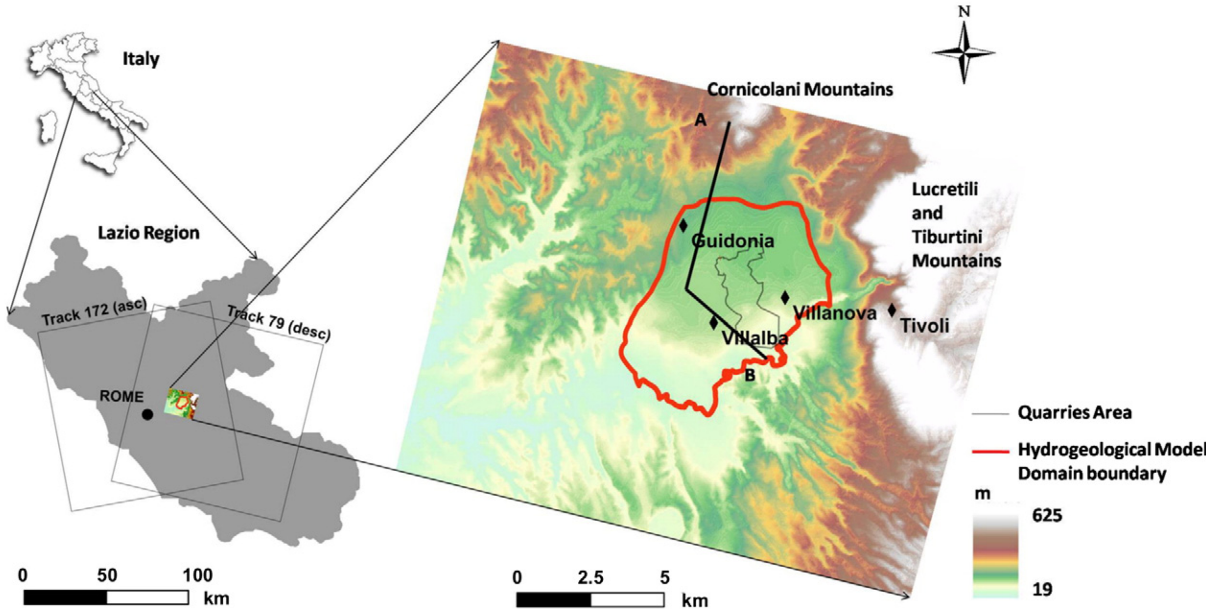

Fig. 1. Location of the Acque Albule Basin. Ascending and descending ERS/ENVISAT frames are outlined in black. Region of interest is enlarged in the right figure. A–B cross-section is represented in the geological sketch of Fig. 7.

Arnaud, 1995, 1993; Massonnet, Feigl, Rossi, & Adragna, 1994; Massonnet et al., 1993; Salvi et al., 2004) has provided over the last decade an incomparable stimulus to the study of such ground deformation processes. The opportunity to retrieve extensive displacement information over large areas with a spatial resolution of a few metres and a millimetre accuracy has allowed analyses at an unprecedented level of precision (Amelung, Galloway, Bell, Zebker, & Laczniak, 1999; Bock, Wdowinski, Ferretti, Novali, & Fumagalli, 2012; Burbey, 2002; Damoah-Afari, Ding, Lu, & Li, 2008; Fruneau & Sarti, 2000; Heleno et al., 2011; Hoffmann, Zebker, Galloway, & Amelung, 2001; Osmanoğlu et al., 2011; Raucoules, Colesanti, & Carnec, 2007; Raucoules et al., 2009; Tesauro et al., 2000). Furthermore, the availability of SAR data archives in some areas since 1992 represents a great opportunity to explore past processes and to analyse them, taking advantage of the most recent evidence and with the most advanced scientific knowledge of the subsidence process.

Obtaining information on ground or building displacement is a key feature for performing detailed and quantitative evaluations of the state of subsidence processes, but several additional studies are required to gain a comprehensive knowledge of the mechanism controlling such processes, especially for the purposes of prediction and assessment of future expected events. Recent studies have focused on the investigation of relationships between the subsidence process and geological, geotechnical and hydrogeological features of the area to shed light onto the expected future evolution of the instability process, thus supporting sustainable management (Bru et al., 2013; Budhu & Adiyaman, 2010; Raspini, Loupasakis, Rozos, & Moretti, 2013; Tomás et al., 2010).

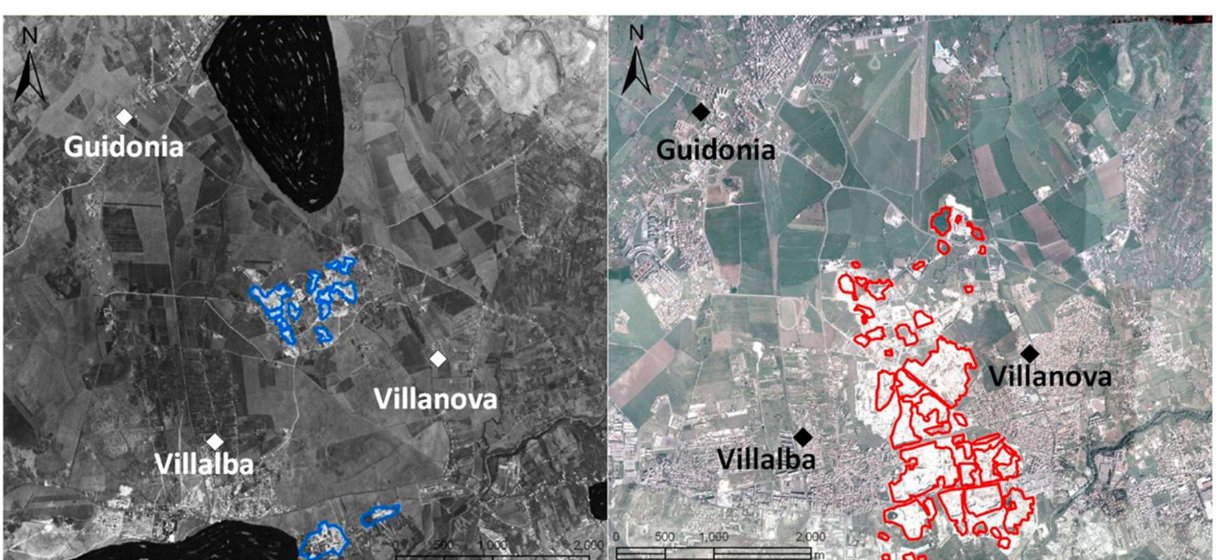

Fig. 2. Evolution of the quarries activities in the plain. The left orthophoto represents the plain in 1954: the perimeter of each pit is shown in blue; some obscured areas are depicted such as the Guidonia airport to the north, as required by the military regulations at the time. The right orthophoto represents the plain in 2005: the perimeter of each pit is shown in red. It is clear the huge expansion of the quarries area.
Modified from Floris et al., 2014).

This study follows the above-described approach, thus focusing also on the impact of human actions and groundwater exploitation on the subsidence process and its effects on buildings and infrastructures.

The study area is located between the municipalities of Tivoli and Guidonia in the Province of Rome (Lazio Region, Central Italy) where open pit travertine mines and hydrothermal waters represent the main economic activities (Fig. 1).

This area, located in the hinterlands of Rome, has been affected by urban development during recent decades. After the recent edification of the area, structural damage to buildings has been recorded since the mid-1980s, with a strong intensification at the beginning of the 2000s, sometimes leading to the evacuation of houses and public buildings. The damages were mainly caused by a generalised subsidence characterised by differential settlements of the buildings.

In this paper, to better understand the observed processes, we first describe a detailed geological model obtained by interpolating data from several available and purposely drilled boreholes and the 1954–2008 piezometric variations reconstructed through a numerical

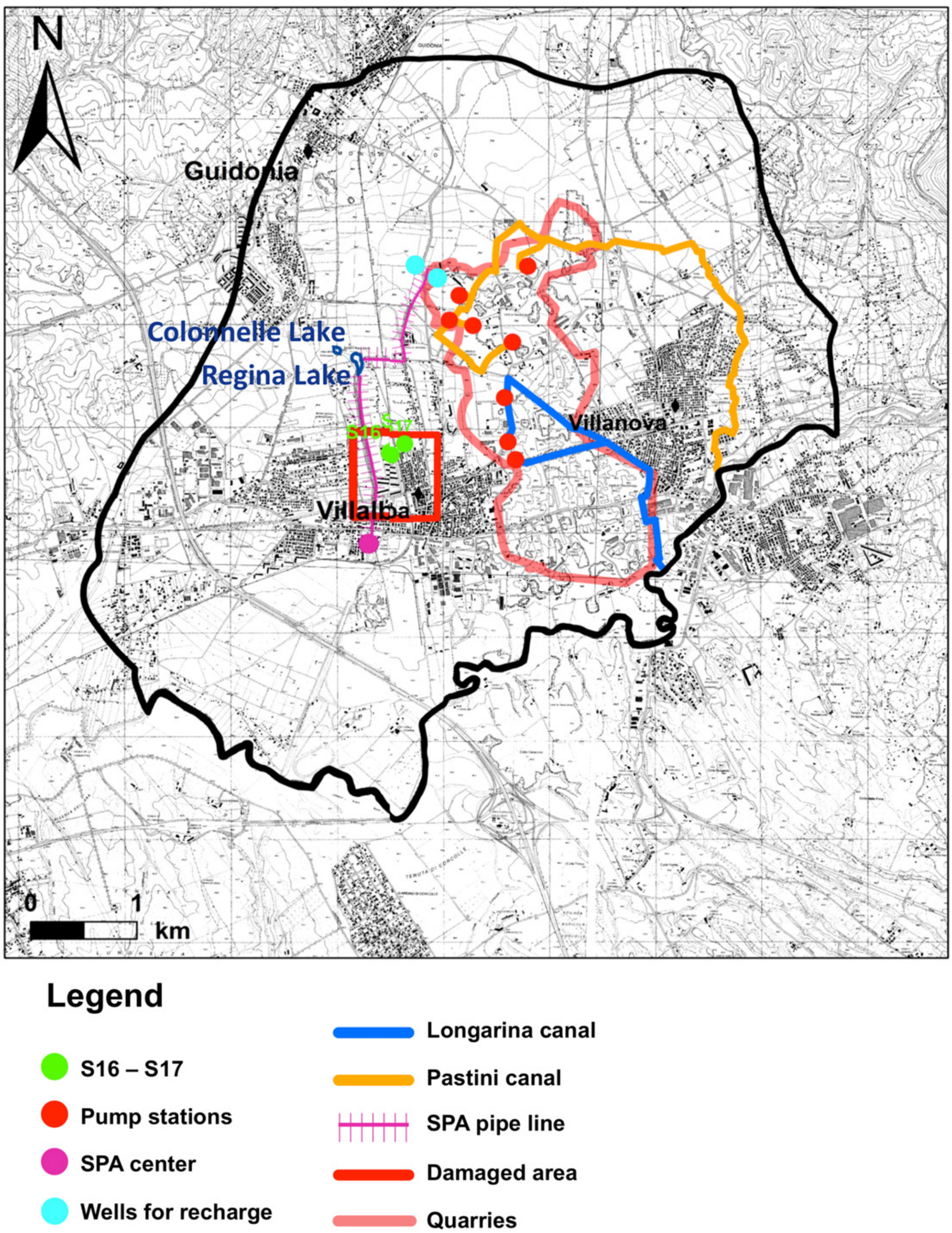

Fig. 3. Location of the main features in the area of interest. The black polygon identifies the study area (and the hydrogeological model boundaries). The light red polygon identifies the quarry area while the red box bounds the urbanised area which has suffered major structural damage. Within the damaged area, two boreholes (S16 and S17) host multi-level electrical piezometer systems (green circles). The eight red circles identify the quarries applying dewatering programmes and the drained water are channelled in the Longarina canal (blue line) or Pastini canal (orange line). The two circles in light blue localise the wells used for the recharge plan, the pink circle identifies the SPA centre while the pink line the related canal. Finally, in the west, the Colonnelle lake and Regina lake are depicted in blue.

Table 1
Total volume of water drained from the quarries to the two canals.

	Pastini canal m^3/s	Longarina canal m^3/s	Total m^3/s
1998	0.64	1.520	2.150
2006 Capelli and Mazza (2006)	0.797	1.634	2.431
Jan 2008	1.574	1.634	3.208
Feb–Mar 2008 La Vigna, Mazza, and Capelli (2013)	1.752	2.546	4.298

model based on previous surveys. We then quantify the subsidence process affecting the overall area from 1992 to 2010 using the Advanced DInSAR (A-DInSAR) methodology, combining the ERS-1/2 and Envisat interferograms from the ascending and descending tracks. Finally, we discuss the causes and time evolution of the observed subsidence, focusing on specific areas of the basin, where the availability and the detail of all of the above information have allowed us to better understand the observed phenomenon and its relationships with the considered environmental variables.

2. Study site

The study area, known as Acque Albule Basin, is situated to the east of Rome, in central Italy. With a surface of approximately 30 km^2, it is mostly urbanised. The territory is quite flat, with elevations gently decreasing (Fig. 1) from approximately 80 m a.s.l. in the north to approximately 40 m a.s.l. in the south.

The primary industrial activity of this area is Travertine quarrying, performed since the ancient Roman age; after the Second World War, this activity increased, thus involving a wide portion of the central part of the basin (Fig. 2).

Floris, Bozzano, Strappaveccia, Baiocchi, and Prestininzi (2014) analysed the evolution of human activities in the plain from 1954 to 2005 through a multi-temporal analysis of photographs and orthophotos of the area. The analysis showed that the quarry areas increased from 0.4 km^2 (1954) to 2.8 km^2 (2005) and also showed a progressive deepening of the quarry floors, from 14 m (1993) to 18 m (2005) below the original ground level. The estimated total volume of travertine quarried from 1954 to 2005 is approximately 50 mm^3.

Due to the local hydrogeological setting, the deepening of travertine extraction implies significant water pumping to keep the water table below the bottom of the quarries. Considering the activities of the quarries and the related dewatering, additional information was collected about the piezometric features and the water extraction in the area over recent years.

Piezometric levels under undisturbed conditions were derived from Lombardi (2005) using piezometric measurements taken in 1969 when quarrying activities were not particularly intense and no significant water pumping was necessary. The results showed that the piezometric levels were located in proximity to the topographic surface.

Piezometric measurements taken on the plain were collected for the years 1994, 1998, 2003, 2006, 2007 and 2008.

Furthermore, in 2006, the CERI (Research Centre on Prediction, Prevention and Mitigation of Geological Risks of the "Sapienza" University of Rome) installed four multi-level electrical piezometers in two boreholes (S16 and S17) (Fig. 3) located close to the open pit area. The piezometric heads show a downward trend during the time interval 2006–2008, attributed to the increased pumping of water from the nearby quarries. In March 2007, the CERI research group, in coordination with the regional authorities, measured the perimeter of each pit, its piezometric level, the quarry floor elevation and the location and characteristics of the active pumps. Among the 19 active and inactive quarries examined, eight quarries that apply dewatering programmes were identified (Fig. 3).

Regarding the volumes of water extracted to allow travertine mining, the data show a progressive increase in pumping over time. Lombardi (2005) estimated a flow rate of 1 m^3/s in the 1970s.

Flow measurements in the canals (Fig. 3) built to transport the water drained from the quarries to the Aniene River are available only since 1998 (Table 1).

The continuous pumping from the quarries has resulted in the progressive reduction of the flow from two springs, Regina Lake and Colonnelle Lake (well known as Acque Albule springs), whose thermal waters are used by several SPA centres, which are the second source

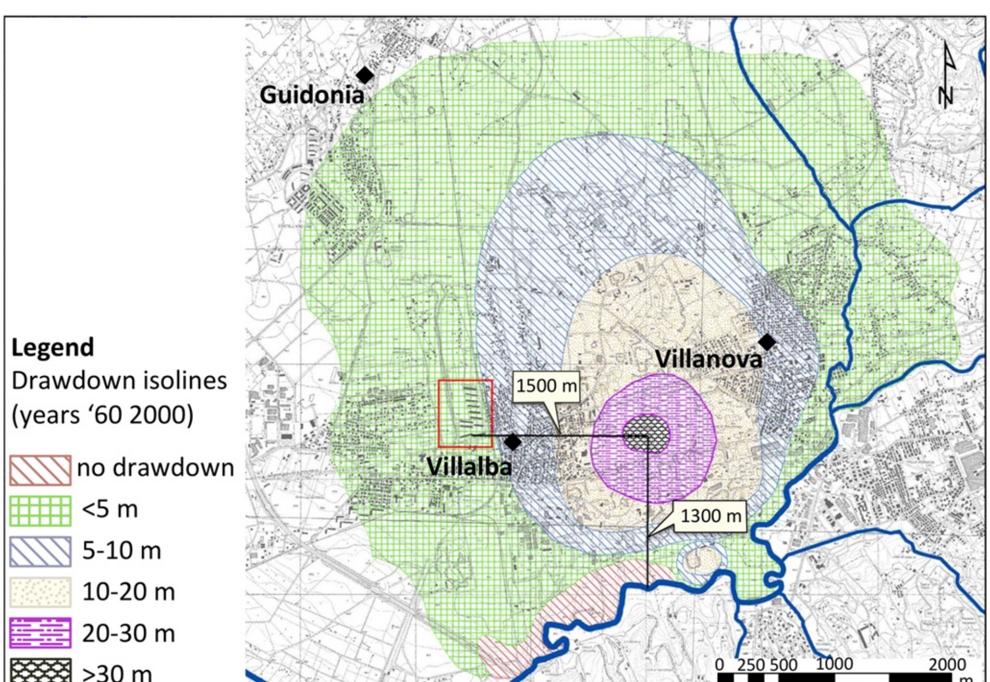

Fig. 4. Groundwater level variation between 1960s and 2000 according to Bono (2005). The red box indicates the most damaged area.

of income for this area. Since July 2007, an artificial recharge of 0.5 m^3/s was activated by the Regional Civil Protection Department with the purpose of raising the water level of Regina Lake. The plan consists of two wells, located 1.4 km north of the lake, which extract a flow of 0.25 m^3/s each. (circles in light blue in Fig. 3) This water is fed into Regina Lake through an underground pipeline (Prestininzi, 2008).

A careful examination of the available data shows that a generalised lowering of the water table affects a wide portion of the Acque Albule Basin, whereas a more significant dewatering (and related piezometric level lowering) involves the areas surrounding the travertine quarries. The piezometric map of Bono (2005) shows a decrease in groundwater level of between 5 and 10 m in the Villalba area in 2005 (Fig. 4), where at present time major damages to structures occurred (Figs. 3 and 4), whereas in the areas of the quarries (Fig. 3), that decrease is up to 30 m (Fig. 4).

2.1. Geological and geotechnical settings

The Acque Albule Basin is a morpho-tectonic depression, whose formation and development is related to the Plio-Quaternary activity of strike-slip tectonic elements (Fig. 5). The basin is bounded to the north and east by calcareous ridges (Cornicolani, Lucretili and Tiburtini Mountains) and to the west and south by the distal slopes of the Colli Albani volcanic edifice and the hilly roman area, both composed of pyroclastic deposits. The Aniene River, one of the left tributaries of the Tiber River, flows from NE to SW and marks the southern margin of the basin.

The morpho-tectonic depression, whose bedrock features Meso-Cenozoic limestone, hosted the deposition of Plio-Pleistocene alluvial, lacustrine and volcanic deposits. These deposits are in turn covered by a thick (up to 80 m) travertine, well known since the Ancient Roman age by the name of *Lapis Tiburtinus*. This travertine cover, whose precipitation and growth occurred in several phases between 115 and 130 thousand years ago (Billi, Valle, Brilli, Faccenna, & Funiciello, 2007; Faccenna, Funiciello, & Mattei, 1994; Faccenna et al., 2008), is strictly related with a deep hydrothermal circulation into the Meso-Cenozoic limestone. The travertine is primarily composed of thick, cemented banks with variable degrees of porosity and jointing. Palaeosol levels, clayey layers and karstic cavities and conduits locally interrupt the continuity of the travertine plateau.

A discontinuous cover of a weakly cemented up to loose travertine, composed of clasts interspersed in a sandy–silty matrix, marks the last phase of travertine deposition.

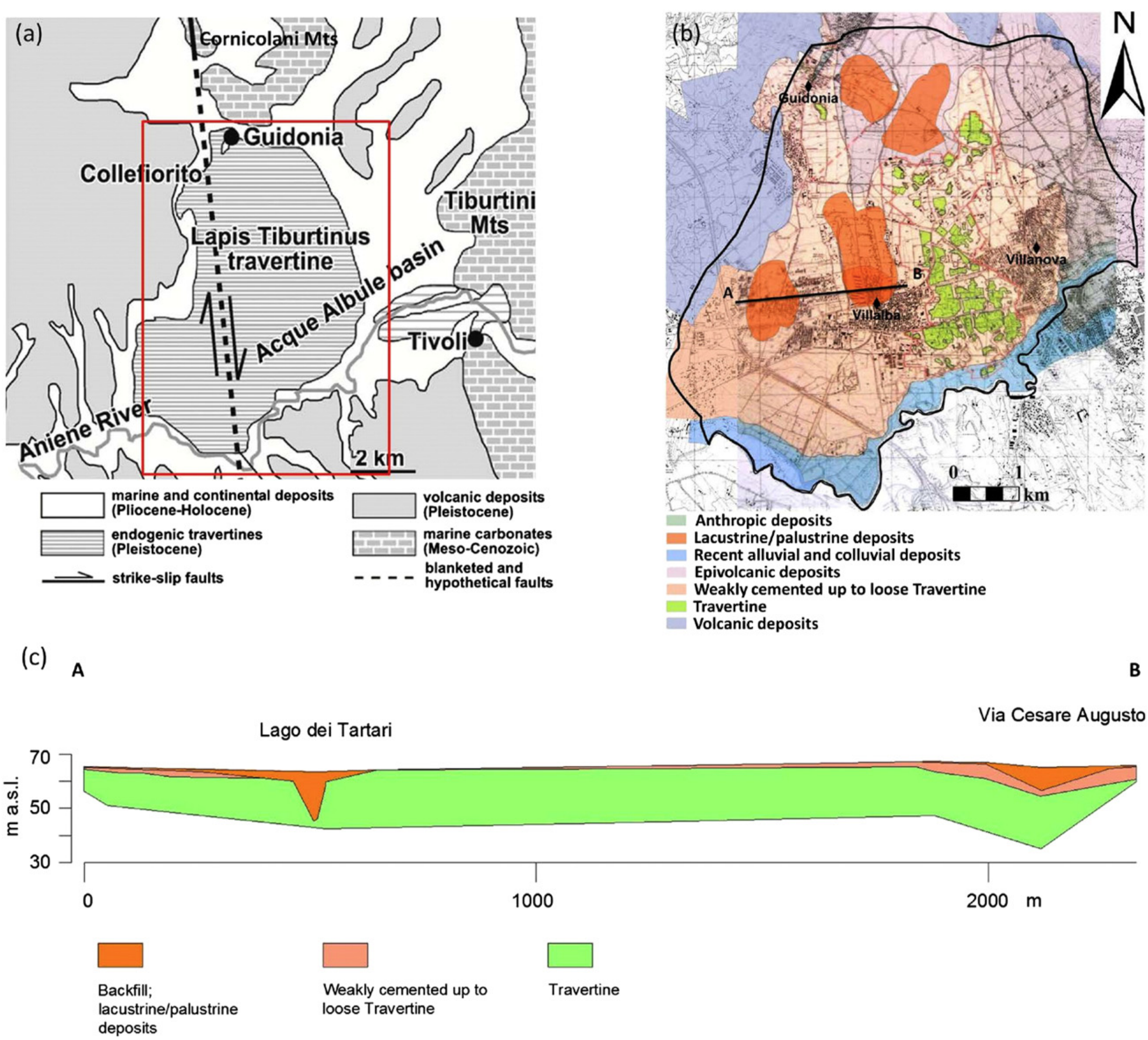

Fig. 5. In (a) we show the geological map of the study area including the Acque Albule basin (from Faccenna et al., 2008). The red box in (a) represents the area in (b) where the geological map of the Acque Albule Basin is shown (Funiciello, Faccenna, De Filippis, & Rossetti, 2005, modified). In Fig. 5b geology is overlaid on a topographic map (original scale: 1:10,000). In (c) the geological profile along AB, is showed.

Finally, the karst collapses in the uppermost part of the travertine sequence caused the recent formation of morphological depressions, which hosted a lacustrine–palustrine environment with the deposition of sandy silts, clay–loam (with high percentage of organic matter) and peats immediately below the present ground level.

The above geological reconstruction, schematically represented in Fig. 5c, highlights complex vertical and lateral relationships among markedly different lithologies (i.e., cemented travertine, loose travertine and lacustrine/palustrine deposits) in the first 10–20 m below the ground level. The litho-stratigraphic setting of the first metres of the subsoil is then characterised by significant variations both vertically and horizontally. The roof of the travertine is strongly articulated by erosion and karst dissolution, such that it is possible to shift from situations in which the travertine reaches the ground surface to areas in which the most recent lacustrine–palustrine deposits fill previous sinkholes with thicknesses up to approximately 20 m.

To define a reliable geological model up to this depth, 97 borehole stratigraphic logs were collected in a georeferenced database, which allowed us to attain fairly detailed information on the spatial distribution of the different deposits in the study area at different resolutions. A low-resolution geological model (average information density of approximately 3 logs per square kilometre) was constructed at the basin scale, and a high-resolution model (average information density of nearly 1 log per ha) was produced for the most damaged area.

As regards the geotechnical properties, a reference model is based on the results of site and laboratory investigations. Such a model is featured by five litho-technical units: 1) topsoil and backfill; 2) sandy silts, clay–loam (with high organic content) and peats; 3) weakly cemented up to loose travertine (silts, sandy silts and gravels in silty matrix); 4) intensively fractured travertine; 5) travertine banks.

Unit 1 has a very variable thickness (0 to 3 m) and composition; its technical parameters are then difficult to summarise.

Units 2 and 3 are characterised by poor mechanical parameters, especially in terms of shear strength and deformability, as they are loose/low consistent and often highly compressible. These units are indeed very heterogeneous both from a stratigraphic and geotechnical point of view: a detail is reported in Fig. 6 which depicts the stratigraphic log of a borehole in correspondence of one of the filled sink holes (column on the left of the figure), the corresponding litho-technical units labelled from 1 to 4 and the related parameters derived from in situ tests (super-heavy dynamic penetration test — DPSH and piezocone penetration tests — CPTU).

Table 2 summarises the variability ranges of the main geotechnical parameters of units 2 and 3, derived from in-situ and laboratory tests. As regards the main compressibility properties, results from oedometric tests on high-quality samples from units 2 and 3 show values of the coefficient of volume compressibility (m_v) on the order of 10^{-3}–10^{-4} kPa^{-1}, compressibility index (c_c) ranging between 0.33 and 0.58 and re-compressibility index (c_r) ranging between 0.017 and 0.092.

Units 4 and 5 are characterised by high values of unconfined compressive strength (on the order of 50 MPa and 100 MPa for units 4 and 5, respectively) as well as by high values of initial elastic modulus (on the order of 6 and 9 GPa for units 4 and 5, respectively).

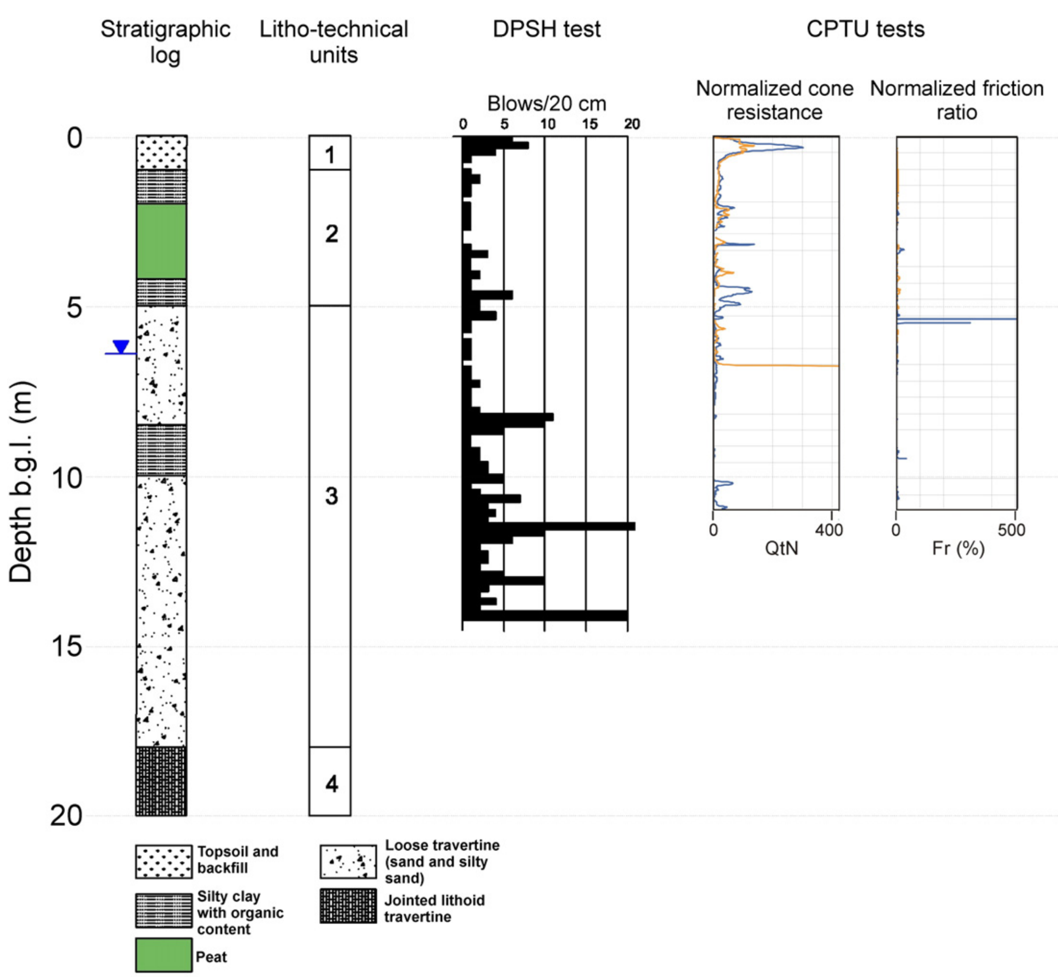

Fig. 6. Stratigraphic and geotechnical settings of the study area, derived from a cluster of geognostic tests performed in a site within the subsidence-damaged area.). From the left to the right: stratigraphic log, corresponding lithotechnical units, results of a DPSH tests (blows/20 cm vs. depth), results of a CPTU log (respectively normalised cone resistance and normalised friction ratio vs. depth).

Table 2
Geotechnical parameters of the litho-technical units. K = permeability; N60 = Nspt (blows/30 cm); Es = Young's modulus; Dr = relative density; Phi′ = friction angle; M = constrained modulus; G_0 = shear modulus; Cu = undrained shear strength; γ = weight per unit volume; * value related to granular layers; ** value related to cohesive layers; c_c = compressibility index; c_r = recompressibility index; $m_{v\,l}$ = coefficient of volume compressibility (loading); $m_{v\,r}$ = coefficient of volume compressibility (reloading).

Geotechnical parameters from CPTU tests													Geotechnical parameters from oedometric tests
Litho-technical units	K (m/s)	N60	Es (MPa)	Dr (%)	Phi′ (°)	M (MPa)	G_0 (MPa)	Cu (kPa)	γ (kN/m^3)	c_c	c_r	$m_{v\,l}$ (kPa^{-1})	$m_{v\,r}$ (kPa^{-1})
Unit 2 (clays, silts, silty-sands)	$2.35 \times 10^{-6}/2.87 \times 10^{-8}$	3–7	1.4–43.6	27–35*	31–35*	3.3–33	11.8–41.1	30.8–70.8**	15.2–16.8	0.335	0.018	7.0E−04	3.5E−05
Unit 2 (Peat and organic clay)	6×10^{-9}	2	0.1			15	8.5	15	16.5	0.581	0.092	1.0E−03	1.6E−04
Unit 3 (sand, silty sands, gravels)	5.55×10^{-5}	12–20	47.2–58.7	43–53	37–39	56–73	59–73		17.5–18.1				
Unit 3 (silts, sandy silts)	$5.86 \times 10^{-6}/8.40 \times 10^{-8}$	3–12	2.6–43.8			3–16	14–37	25–63	15.8–16	0.358	0.017	6.7E−04	3.2E−05

2.2. Hydrogeological setting

The complex geological setting described above determines the complex multi-level groundwater circulation in the region (Fig. 7). Specifically, the Meso-Cenozoic limestone (symbol 6 in Fig. 7) hosts a deep aquifer fed laterally by the deepest part of the surrounding carbonate ridges, outcropping east and North-East of the basin (Fig. 5). The groundwater at these levels is thermalised due to the rise of deep fluids from the supply system of the Colli Albani volcanic complex, which outcrops southward. The aquifer is confined at the top by clayey–sandy Pliocene and Pleistocene deposits (symbols 5 and 4 in Fig. 7) acting as an aquitard/aquiclude and therefore providing a piezometric level that is at times higher than the ground level.

The aquitard separates the deep aquifer from the most superficial one hosted in the travertine plateau (symbol 3 in Fig. 7), which is directly fed by rainfall (characterised by an effective infiltration of 275 mm/y) and laterally fed by the above mentioned surrounding carbonate ridges (with an estimated flow of 4 m^3/s). Furthermore, this superficial aquifer is partially fed by the upwelling of thermalised waters (and gas) coming from the deep aquifer and passing through the tectonic discontinuities that drove the formation of the basin itself (Boni, Bono, & Capelli, 1986; Capelli, Cosentino, Messina, Raffi, & Ventura, 1987; Capelli, Mazza, & Gazzetti, 2005; Faccenna, 1994; Faccenna et al., 2008) (Fig. 5). Several springs with significant discharge, such as Acque Albule, Bretella and Barco springs, demonstrate the huge potential of this aquifer, whose water originates from the ascent of hydrothermal fluid from the deeper aquifer. Therefore, with the travertine aquifer, the Aniene forms a “global system” in which the two hydraulic units are characterised by continuity and reciprocal exchanges (Boni et al., 1986; Bono, 2005).

The hydrodynamic parameters of the superficial travertine aquifer were estimated by pumping tests and recovery tests. The estimated hydraulic conductivity is $5.3°10^{-3}$ m/s with a specific yield of 0.01, and the estimated transmissivity is $2.7°10^{-2}$ m^2/s (Brunetti, Jones, Petitta, & Rudolph, 2013; Carucci, Petitta, & Aravena, 2012; Petitta, Primavera, Tuccimei, & Aravena, 2011).

2.2.1. Groundwater numerical modelling

We investigated the evolution of the underground water circulation using a 3D groundwater flow model, which was developed using Visual MODFLOW 4.2 (Waterloo Hydrogeologic Inc., 2006) as pre- and post-processors of the finite-difference code MODFLOW2005 (Harbaugh, 2005) to reconstruct the “time history” of the dewatering process over time and space. In this paragraph some details about the hydrogeological model used to infer the subsidence process are presented.

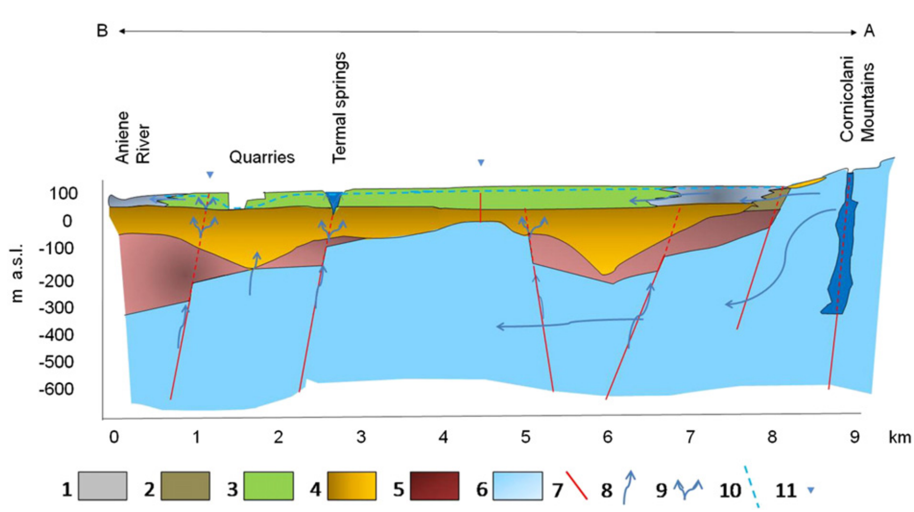

Fig. 7. Cross sections A–B are located on Fig. 1. 2D view of the geological and hydrogeological conceptual models for the Acque Albule Basin. Key to legend: 1) recent alluvial and colluvial deposits; 2) Debris; 3) Travertine and lacustrine/palustrine deposits; 4) Pleistocene alluvial, lacustrine, and epivolcanic deposits; 5) Pliocene marine deposits; 6) Carbonatic bedrock; 7) Fault; 8) Flow direction; 9) Groundwater overspill; 10) Water table level; 11) Confined water table level.
Modified after Capelli, Mazza, and Taviani, (2005).

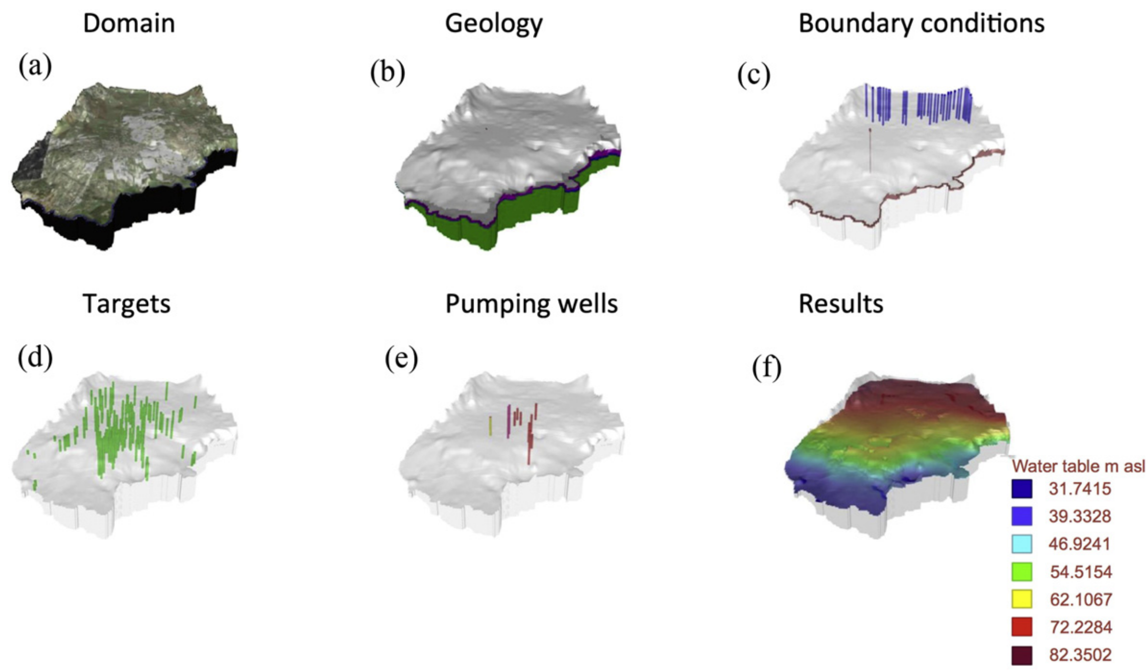

Fig. 8. Processing chain for obtaining the 3D hydrogeological finite-difference model. The model domain has been defined and 3D geology has been derived from 97 boreholes. Once boundary condition has been defined, the model has been calibrated on the basis of available data (targets). Finally, the "time history" of the water levels has been derived.

The Acque Albule model was calibrated and validated with respect to the hydraulic conductivity field following a two-steps procedure: i) in steady-state conditions, the model has been calibrated using the piezometric heads observed in 1950 (Maxia, 1950). Such a piezometric field can be considered as representative of quasi-natural conditions, i.e. prior to well exploitation; ii) validation of the calibrated hydraulic conductivity pattern has been performed in transient model considering both the piezometric field reconstructed after the 2003 survey (Petitta & Del Bon) and the piezometric head evolution from 1954 to 2008, which was substantially driven by pumping and thermal activities.

The domain of the model covers 32.5 km^2 and circumscribes the travertine aquifer system (Fig. 8a), including the extraction area of the quarries, the area affected by subsidence and the urban settlements of Villanova, Villalba and Guidonia.

The average size of the cells is 50 × 50 m, with a grid refinement of up to 10 × 10 m in the areas of the quarries, Regina Lake and Barco and Bretella springs, to better represent the features of the groundwater flow in the areas of interest. Therefore, the final grid accounts for 309 rows and 262 columns.

Following Brunetti et al. (2013), the model considers three hydrostratigraphic units (i.e., three layers, Fig. 8b). The first layer merges together the first and second units of the geotechnical model previously described (Fig. 6 and Table 2), the second layer corresponds to the third unit, and the third layer groups the fourth and fifth geotechnical units of that model (see Section 2). The surfaces bounding the three layers have been obtained by the interpolation of the stratigraphic data, using the Inverse Distance Weighted method (IDW). The topography was derived from a digital elevation model with a spatial resolution of 20 m, obtained by cartography at the scale 1:2000 kindly provided by the Municipalities of Guidonia and Tivoli (Lazio Region).

The main groundwater inflow to the travertine aquifer along the northern margin (Fig. 8c, blue bars) was simulated by a constant inflow boundary condition equal to the lateral recharge from the Cornicolani and Lucretili mountains (4 m^3/s, Boni et al., 1986; Capelli et al., 1987; Carucci et al., 2012; Brunetti et al., 2013).

A constant head boundary condition equal to the hydrometric heights was assigned to the cells, corresponding to the main thermal discharge zone of Regina Lake and the Barco and Bretella springs. Hydrothermal water flowing into the system from the deep carbonate aquifer beneath Regina Lake was represented via a constant head boundary condition assigned to the second and third layers. Constant head boundary conditions have been assigned to the cells of the top layer corresponding to the Aniene River (Fig. 8c, magenta line), as this surface body is supposed to be in perfect hydraulic contact with the aquifer: as a consequence along the southern margin the Aniene hydrometric level coincides to the hydraulic potential of the aquifer. No-flow boundaries were assigned along the eastern and western sides of the domain, according to the geological model by Brunetti et al. (2013). In such model the travertine aquifer is recharged by underground contribution from aquifers hosted in the Cornicolani Mountains (North) and Lucretili–Tiburtini Mountains (North-East) and also thanks to surficial recharge. The geological formations located East and West host local aquifers not interacting with the travertine aquifer (see Fig. 5a and b).

Effective infiltration was considered uniform over the whole domain. In the steady state, undisturbed conditions, the effective infiltration was assigned to the uppermost active cells as a constant flux of 274 mm/y (Brunetti et al., 2013). In transient conditions, the same effective infiltration recharge was assigned only for six months of the year, from November to April, and it was considered to be negligible for the remaining months based on the rainfall pattern of central Italy outlined by Dragoni (1998).

The location of the monitoring wells, including all the surveys taken into account for the model calibration and validation, is depicted in Fig. 8d, as well as the pumping wells (Fig. 8e). Finally, an example of

Table 3
Calculated hydraulic conductivity.

Zone	k_x (m/s)	k_y (m/s)	k_z (m/s)
Litho-technical unit 1 and 2	$1.5 \cdot 10^{-7}$	$1.5 \cdot 10^{-7}$	$1.5 \cdot 10^{-7}$
Litho-technical unit 3	$3 \cdot 10^{-4}$	$3 \cdot 10^{-4}$	$3 \cdot 10^{-4}$
Litho-technical unit 4	$4 \cdot 10^{-2}$	$4 \cdot 10^{-2}$	$4 \cdot 10^{-2}$
Litho-technical unit 5	$5 \cdot 10^{-4}$	$5 \cdot 10^{-4}$	$5 \cdot 10^{-4}$
Aniene River bed	$2 \cdot 10^{-4}$	$2 \cdot 10^{-4}$	$2 \cdot 10^{-4}$
Vertical conduit	1	1	1
Aniene deposits	$1.21 \cdot 10^{-5}$	$1.21 \cdot 10^{-5}$	$1.21 \cdot 10^{-5}$

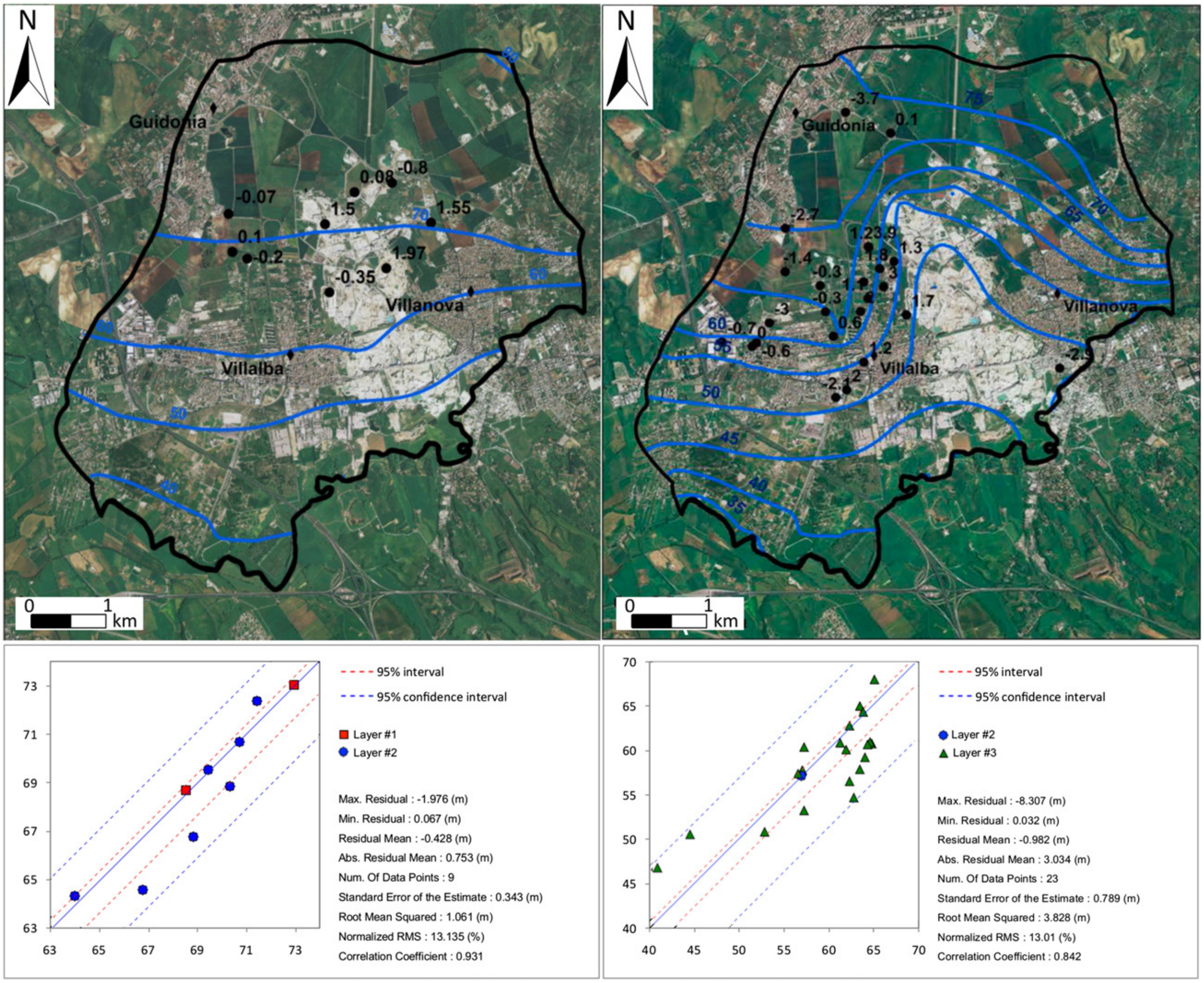

Fig. 9. Piezometric surface calculated for the year 1950 (undisturbed conditions, left) and for the year 2003 (exploitation condition, right); the label of points indicate difference between the piezometric height measured and that for the simulated targets. The related scatter plots "simulated values vs. observed values" are presented in the lower part of the figures.

the water table location simulated during the transient condition is shown in the same figure, panel f.

The model has been calibrated with respect to the hydraulic conductivities considering the undisturbed flow conditions represented by the piezometric field prior to 1954, when the mining activities were concentrated in a very limited area (Floris et al., 2014). The targets, i.e., the observed values, used for calibration were taken from Maxia (1950). The calibration process was performed on the hydraulic conductivity of the travertine, by using horizontal hydraulic conductivity (k) and transmissivity (T) derived from the pumping test described

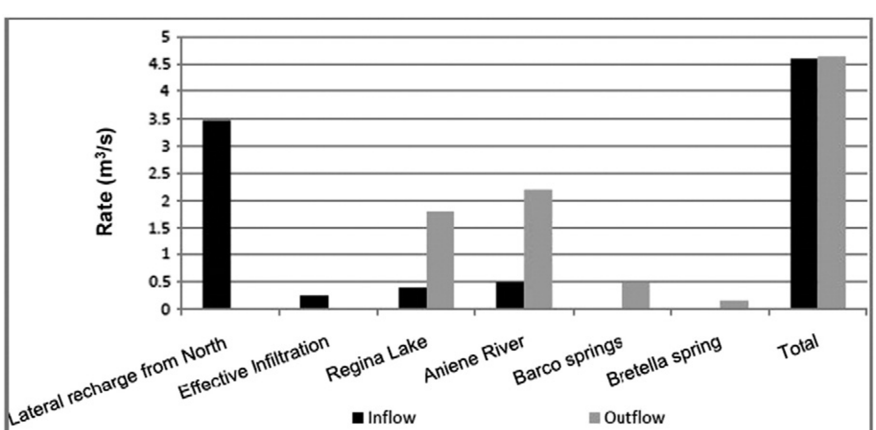

Fig. 10. Inflow and outflow rates in steady state condition.

above. Specifically, five different classes of hydraulic conductivity have been defined within a range from 10^{-7} m/s to 10^{-3} m/s. A higher conductivity value, $7°10^{-2}$ m/s, was assigned to specific areas: i) the northern and north-eastern boundaries where the travertine aquifer is fed by the inflow from the Cornicolani and Lucretili carbonate aquifer; ii) along the north–south fault passing through Regina Lake; iii) in the quarries area, with a general trend reflecting the jointing of travertine, as explicated by Capelli, Mazza, and Taviani (2005). Finally, a very high conductivity value ($k = 1$ m/s) was assigned to a conduit that preferentially drives hydrothermal fluids from a deep aquifer, directly feeding Regina Lake.

The performed calibration led to the values of hydraulic conductivity summarised in Table 3. The agreement between the model and the observation (MAE = 0.753; RMSE = 1.06 m) in terms of piezometric heads (Fig. 9) left) has been considered satisfactory for the purposes of the present paper. The resulting mass balance is shown in Fig. 10.

The model in transient condition run as validation step aimed at simulating the piezometric head evolution from 1954 (prior to exploitation) to 2008. All piezometric data available and described in Section 2.2 were used as the targets for the calibration. The elevation of the pit floors for the years 1954, 1985, 1993, and 2001 derived from Floris et al. (2014) were considered indicative of the piezometric

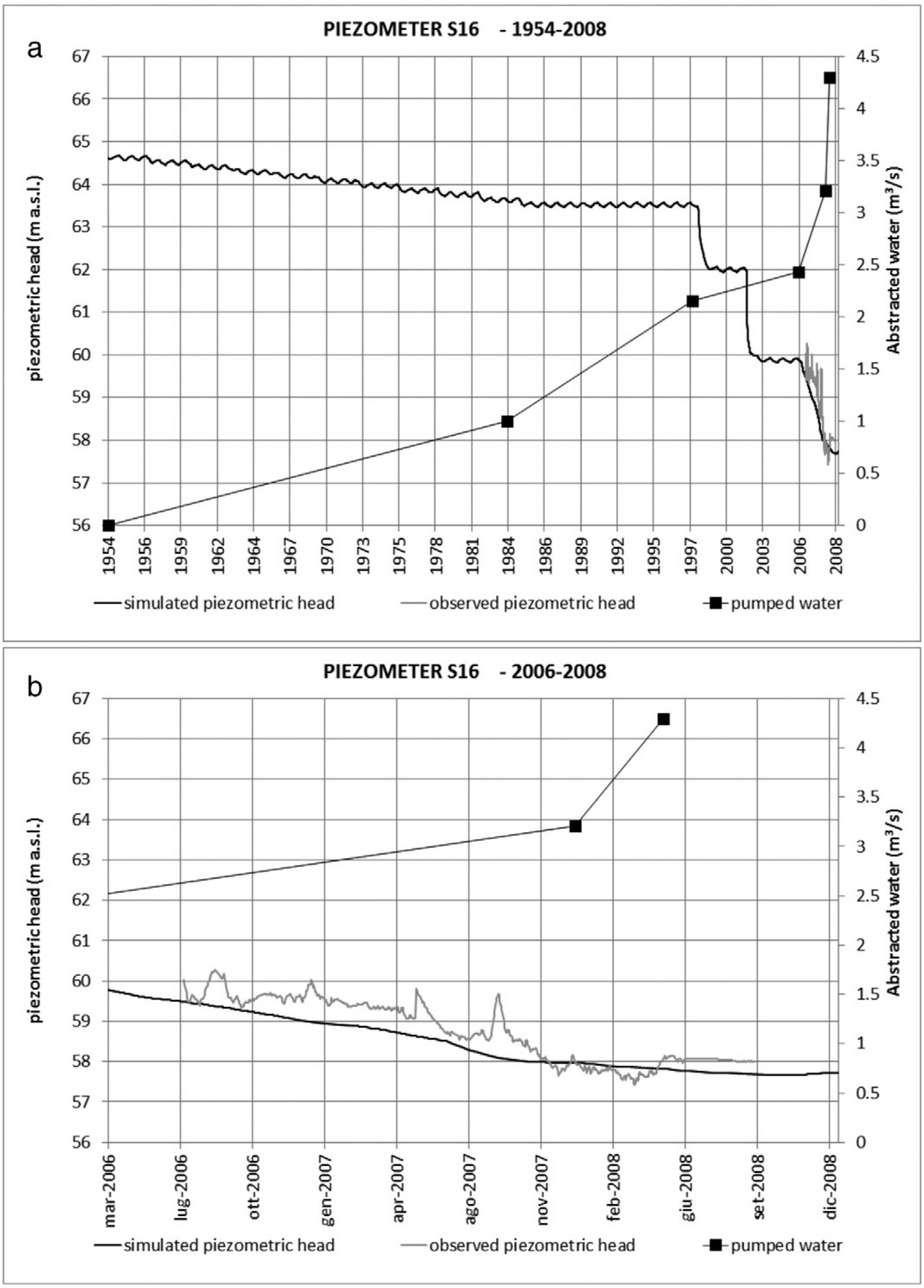

Fig. 11. Time series of groundwater elevation at S16 compared with the total pumped water: (a) simulated water level in the whole period (1954–2008); (b) Zoom on the period between 2006 and 2008.

heads necessary to allow the mining activity. Both the initial conditions of the piezometric heads and the conductivity values assigned to the model were derived from the previous calibration step. Specific yield has been set equal to 0.01, based on results from pumping tests and recovery tests (Brunetti et al., 2013; Carucci et al., 2012; Petitta et al., 2011).

In order to simulate the abstractions, we considered eight pumping wells corresponding to the main pumping stations that were individuated during the quarry monitoring survey performed in March 2007. The amount of water pumped by each quarry was assumed to be proportional to the number of active pumps. The uncertainty of the extractions from the quarries is primarily due to the uncertainty of the evolution of this budget term during the period between two successive measurements (see Table 1 and Section 2) (Fig. 11).

The pumping station installed at Regina Lake to supply the water demand from thermal activity was simulated through a well that removed water from the domain at a rate of 0.7 m^3/s. Two wells extracting water at a rate of 0.25 m^3/s each were used to simulate the Civil Defence well field. The water extracted through these wells flows into Regina Lake. This feature was embedded into the model via an injection well of 0.5 m^3/s.

We compared observations and modelling results for the piezometers at S16 and S17, at which the installed instrumentations allowed to get head data at daily scale. As an example, Fig. 11a and b show the time series simulated for the piezometers at S16 (location in Fig. 3) compared with the observed values of the piezometric heads.

Transient simulations correctly reproduces the observed decreasing trend: the observed water table lowering from July 2006 to April 2008 is 1.86 m and 2.45 m for S16 and S17, respectively; at the same locations the model computed a decreasing piezometric head equal to 1.66 m and 2.31 m, respectively.

In order to check also the ability of the model to reproduce the spatial distribution of the piezometric heads, modelling results relative to 2003 have been compared to the observations gathered during the piezometric survey of the same year (Petitta & Del Bon, 2003). The comparison of the observed and simulated heads (Fig. 9, right) shows good agreement for the points in the area of damage and the area of interest; the calculated values at the targets located far from the central part of the model show higher values of residuals (mean error $= -0.98$ m, standard deviation $= 3.8$ m and correlation coefficient $= 0.84$).

3. Advanced DInSAR analyses

Advanced Differential Interferometric SAR (A-DInSAR) analyses were performed to acquire information regarding past displacements that affected the ground surface over the entire investigated area beginning in 1992. A-DInSAR is the only technique able to provide quantitative past displacement information with a high spatial density and millimetre accuracy. A-DInSAR techniques can take advantage of more than 20 years of archived SAR images. From this perspective, they represent an important tool for the detection and estimation of past displacements. These techniques have been successfully applied in earth deformation investigation, in particular for urban subsidence (Bock et al., 2012; Burbey, 2002; Damoah-Afari et al., 2008; Heleno et al., 2011; Osmanoğlu et al., 2011; Raucoules et al., 2007).

3.1. Performed analyses

To attain subsidence information distributed as well as possible in time, 198 ERS and Envisat archive SAR images in both the ascending and descending acquisition geometries and spanning from June 1992 to September 2010 (Table 4) have been provided by the ESA in the framework of the CAT-1 project "Geological reconstruction and monitoring in recently urbanised areas affected by subsidence." The SAR data present temporal gaps between the two stacks of images, ERS and Envisat. Specifically, for the ascending geometry, we do not have data from 12/11/2000 through 15/11/2002, whereas for the descending geometry, the temporal gap goes from 19/02/2001 to 09/11/2002. Moreover, the ERS data-stack has a non-negligible time gap in the time interval November 1993–May 1995.

In this study, we obtained ground subsidence measurements using proprietary procedures implemented in SARproz (Perissin, Wang, & Wang, 2011). Specifically, we adopted a hybrid approach based on the PS InSAR (Ferretti et al., 2001) and Quasi-PS InSAR (QPS) techniques (Perissin & Wang, 2012). The classic PS approach uses a single master configuration and the phase is not filtered. The QPS technique is based on a different set of filtered interferograms (multi-master configuration) and it is weighted by the interferometric coherence. The first approach, based on sparse point-wise targets (Persistent Scatterers), is more conservative and more robust, producing more accurate time series. QPS on the contrary, based on highly coherent interferograms, allows retrieving information also on distributed targets, less robust but denser.

Four available data-stacks of images were cropped to extract a 10 km × 10 km subarea, and they were then processed independently by selecting a single master image and by co-registering all slave images with respect to it (Fig. 12).

The analysis was performed through two main approaches:

i) full-site processing that allowed us to derive deformational trends of the entire area; and
ii) local-scale processing on some specific areas of interest, to analyse displacement time series point-by-point, thus also identifying non-linear deformation behaviours over time.

3.1.1. Full-site analyses

For the full-site analyses, PS candidates (PSC) were selected based on a combination of several quality parameters related to radar signal stability, such as reflectivity, Amplitude Stability Index (ASI, i.e., the amplitude coefficient of variation) and the spatial coherence. A network of PSC was created to estimate the preliminary height and velocity parameters to retrieve and remove the Atmospheric Phase Screen (APS). After the APS removal, a second estimation of parameters was performed on a wider set of points, selected based on a spatial coherence and ASI combination criterion. At the end of the PS analyses, all PSs with temporal coherence above a reliable threshold (primarily dependent on the number of images analysed in the data-stack) were selected.

For each PS, the LOS velocity, displacement time series and heights have been computed using a linear deformation trend model. Displacements have been related to reference points located outside the Acque Albule Basin where the bedrock outcrops. The absence of compressible layers allowed us to assume that the geological and geotechnical conditions in this area had prevented the onset of the subsidence process that has occurred in the Acque Albule Basin.

3.1.2. Local-scale analyses

Local scale analyses have been performed on some portions of the basin involved in the dewatering process following the outcomes

Table 4
SAR data sets used in this work: time span, incidence angles θ (degree), azimuth φ (degree) and number of available SAR images N.

InSAR set	Time span	φ (degrees)	θ (degrees)	N
ERS, Track 172 (ascending)	28/4/1993–2/9/2000	344	23	29
ENVISAT, Track 172 (ascending)	16/11/2002–21/8/2010	344	23	51
ERS, Track 79 (descending)	11/6/1992–18/2/2001	161	23	68
ENVISAT, Track 79 (descending)	10/11/2002–15/8/2010	161	23	50

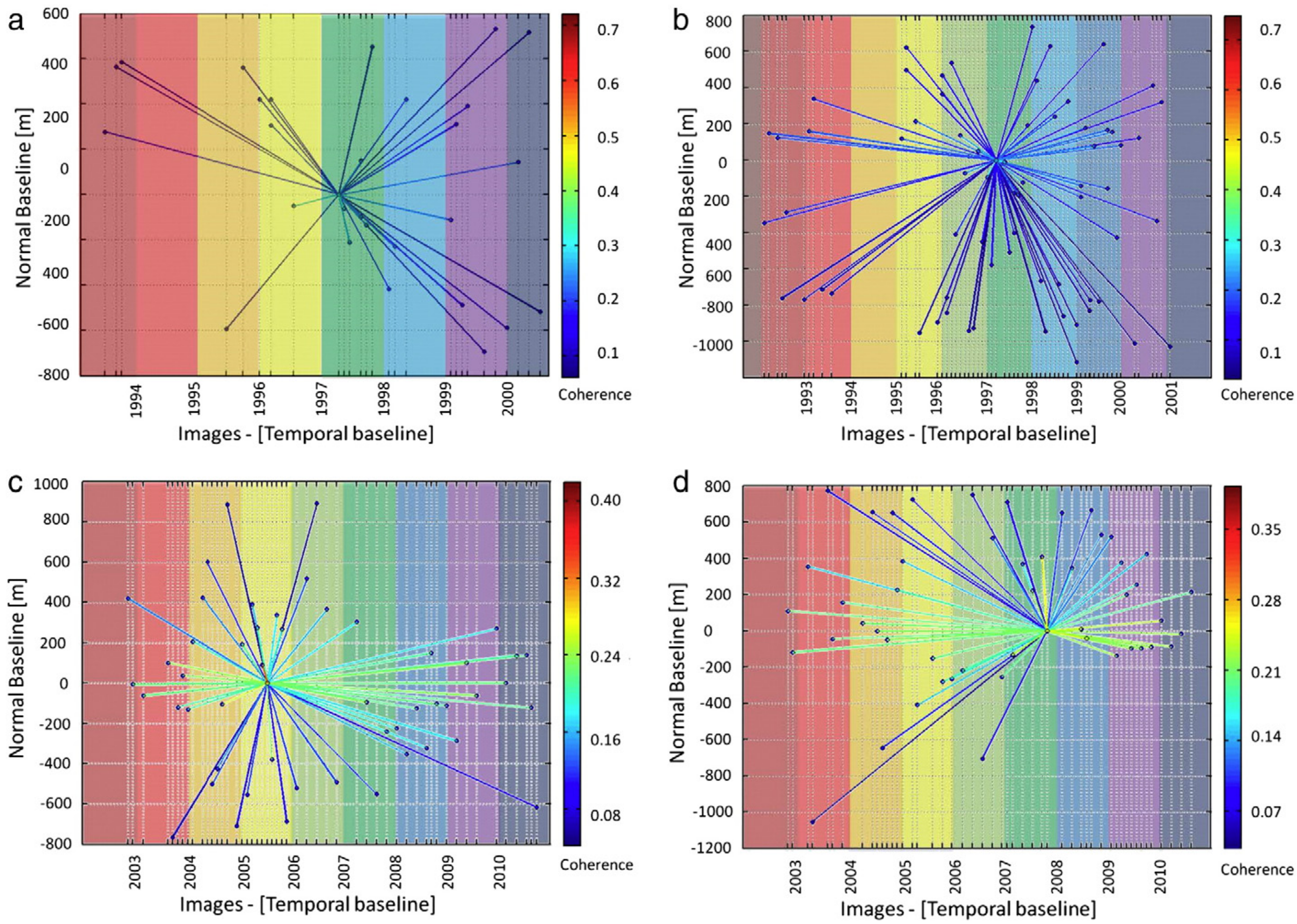

Fig. 12. Graphs used to connect images relating to temporal baseline (X axis) and normal baseline (Y axis). Every dot represents an image, while every line represents an interferogram. Every image is connected to a master one, approximately in the centre of the graph space. Line colours from blue to red show increasing value of spatial coherence. The four datasets are respectively: ERS ascending (a), ERS descending (b), Envisat ascending (c), Envisat descending (d).

derived from the geological setting and hydrogeological modelling described in Sec 2. In particular, the primary objective of the local scale approach was to perform in-depth A-DInSAR analyses characterised by a stronger control on the single PS displacement time series.

We separately analysed some sectors of the basin with an area less than 2 km^2. These sectors have been identified based on a geological–geomorphological criterion: each includes stable areas (where Alban volcanic deposits and/or Plio-Pleistocene marine deposits outcrop) and a portion of the plain where compressible deposits outcrop.

This method helped us to select reference points, which were located in the stable areas mentioned above. PSCs were then chosen based on an ASI threshold value of greater than 0.6. In this approach, we did not perform the estimation and removal of APS as we assumed the atmospheric perturbations were negligible, with a correlation distance of less than 1 km (Hanssen, 2005). In this way, we avoided the risk of losing displacement phase components wrongly considered to be atmospheric artefacts. Moreover, the displacement estimation has been performed via a low pass filter in the time domain, specifically designed to detect and measure non-linear deformation behaviours. As expected, the PSs are primarily located in urban areas.

The final results have been selected by applying a high temporal coherence threshold, thus selecting only pixels characterised by a temporal coherence greater than 0.8 to attain only reliable time series.

3.2. Results of A-DInSAR analyses

The subsidence rates of the full-site processing data are summarised in Fig. 13 (ERS period) and Fig. 14 (Envisat period); to improve the visibility of the results, the PS were averaged within a regular grid (cell dimensions: 50 m × 50 m). In (a) and (b), we show the averaged LOS velocity map obtained for the ascending and descending geometries. Because the results from both geometries were available, the vertical and horizontal components could be derived. The global deformation process expressed a primarily vertical direction of displacement with a negligible horizontal component, as expected for a subsidence process. In (c), the so-derived vertical component of deformation is depicted.

Superimposed on the c map, we also reported the contour map of the thickness of the compressible deposits.

Our next focus is on three specific sectors of the plain whose deformational behaviour is particularly significant to understand the overall investigated process. These sectors, described more in detail (black boxes in Figs. 15–17), are the "Central" sector (which includes the town of Villalba), the "Northern" sector (which includes the town of Guidonia) and the "Western" sector (south-west of the town of Villalba).

The Central sector (Fig. 15a), very close to the open pit area, was affected by average deformation rates ranging from 3 mm/y to 10 mm/y during 1993–2000. From 2003 to 2010, the subsidence rate was greater

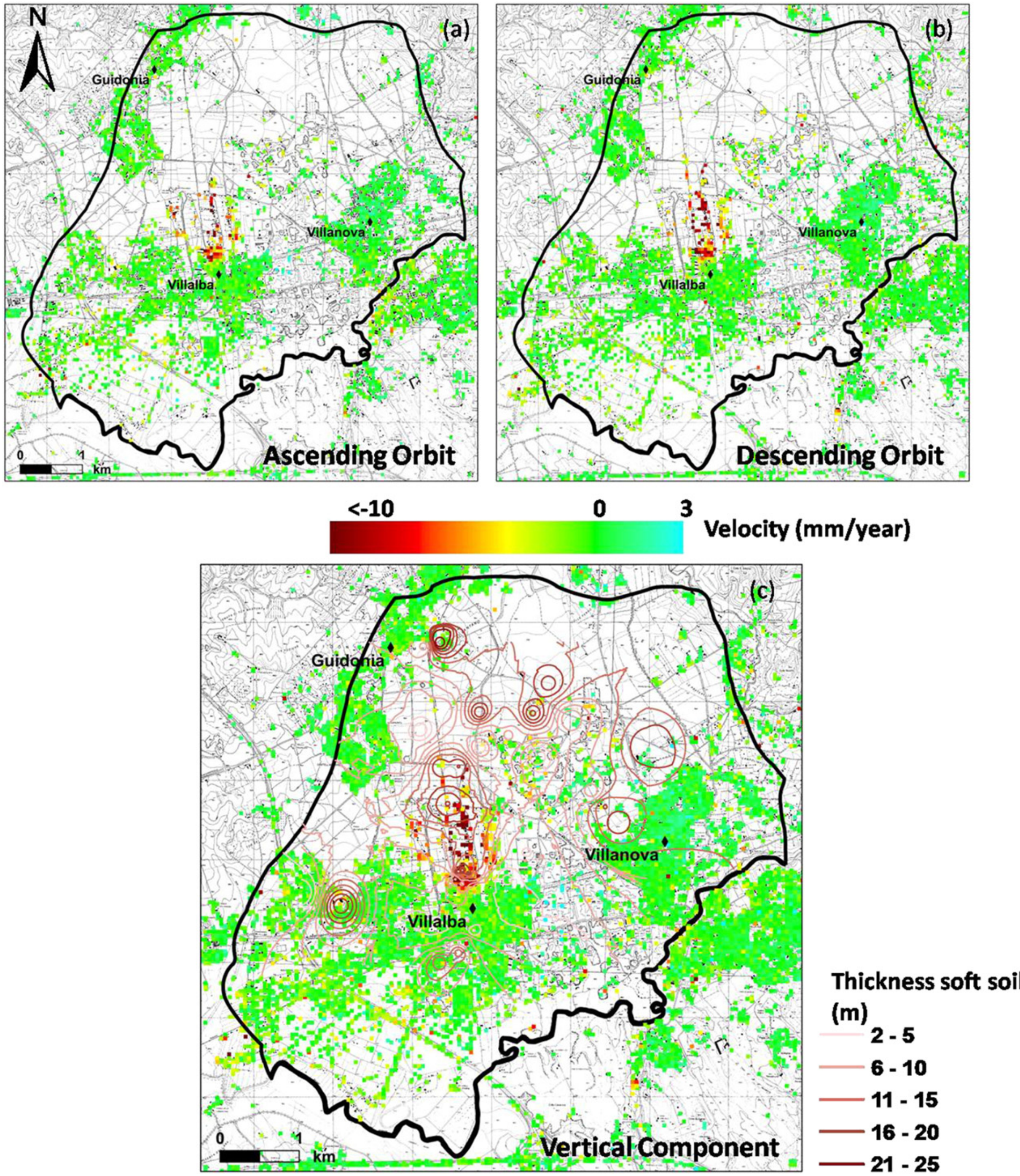

Fig. 13. Average 1993–2000 velocity maps of displacement of the Acque Albule Basin. In (a) and (b) we reported LOS velocities. Vertical component (in millimetre/year) have been extracted using ascending and descending acquisition (c). In LOS displacement maps (a and b), negative velocities (from yellow to red) represent movements away from the satellite while positive velocities (from light blue to dark blue) represent movement towards the satellite. In vertical displacement map (c), negative velocities (from yellow to red) represent downward movements (i.e. subsidence) while positive velocities (from light blue to dark blue) represent upward movements (i.e., uplift). Green points indicate stable areas. In (c) surface geology contours of the compressible deposits is shown. Ground subsidence is clearly visible on vertical deformation map.

than in the previously investigated period and presented an average deformation rate ranging from 10 mm/y to 25 mm/y. In this sector, the thickness of the compressible deposits exceeds 20 m. The displacement time series show a continuity of the process over time, with a slight increase in the rate of subsidence in the Envisat period. The vertical displacement time series and corresponding linear rates of subsidence are presented in Fig. 15b.

The Northern sector (Fig. 16a), located 3 km north of the open pit area, appeared to be stable during 1993–2001, whereas it was subsiding in 2003–2010, with deformation rates ranging between 10 mm/y and 15 mm/y. The vertical displacement time series and corresponding linear rates of subsidence are presented in Fig. 16b.

In contrast with the Northern sector, the Western sector is characterised by stronger urbanisation. A very localised area,

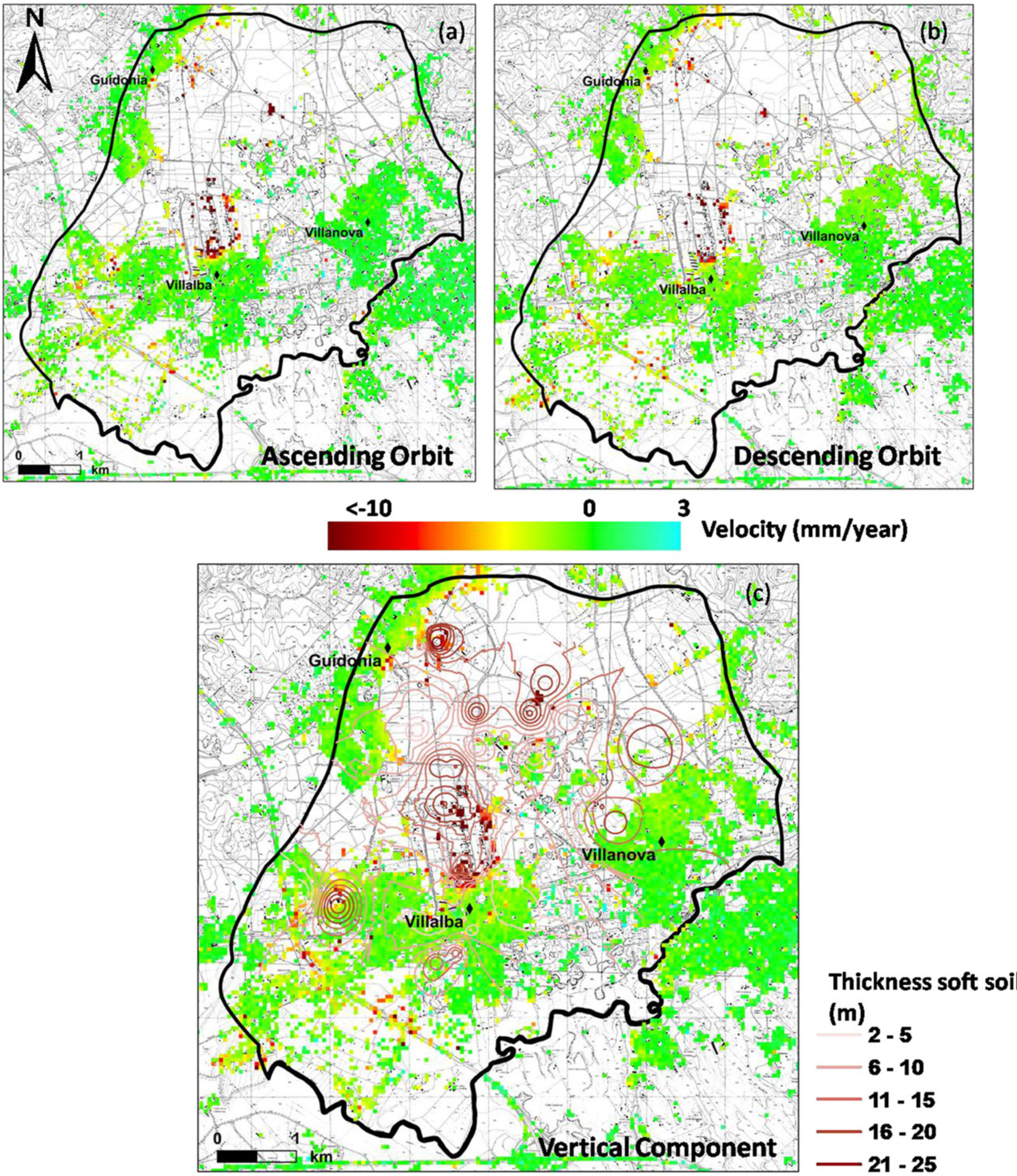

Fig. 14. Average 2001–2010 velocity maps of displacement of the Acque Albule Basin. In (a) and (b) we reported LOS velocities. Vertical component (in millimetre/year) have been extracted using ascending and descending acquisition (c). In LOS displacement maps (a and b), negative velocities (from yellow to red) represent movements away from the satellite while positive velocities (from light blue to dark blue) represent movement towards the satellite. In vertical displacement map (c), negative velocities (from yellow to red) represent downward movements (i.e. subsidence) while positive velocities (from light blue to dark blue) represent upward movements (i.e., uplift). Green points indicate stable areas. In (c) surface geology contours of the compressible deposits is shown. Ground subsidence is clearly visible on vertical deformation map.

distinguished by higher compressible deposit thickness, shows slight subsidence in the ERS data, most likely due to the induced load. However, (Fig. 17), similarly to the Northern sector, the Western sector widely experienced subsidence in 2003–2010, with deformation rates ranging between 5 mm/y and 10 mm/y. The presence of a bowl-shaped area of subsidence highlights the spatial distribution of the compressible deposits, whose maximum thickness (in the centre of this sector, see Fig. 13c) was found in the wetlands and lakes as described in Section 2.1. The vertical displacement time series and corresponding linear rates of subsidence are presented in Fig. 17b.

Otherwise, some remaining portions of the study area had essentially no deformation until 2010. They are located towards the west and the east of the basin. These two areas are located on Albano-volcanic formations and on old Plio-Pleistocene formations and carbonate rocks, respectively. In addition, in some zones within the basin where travertine deposits outcrop, no deformation is detected.

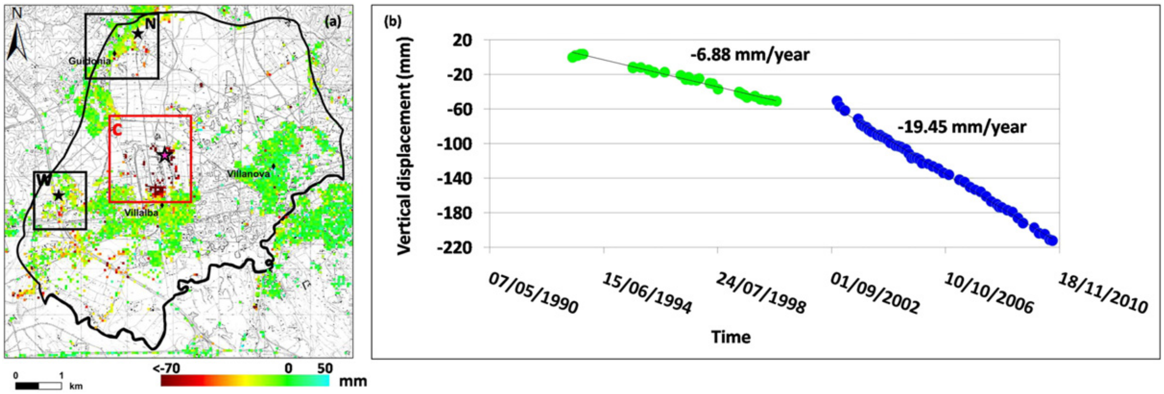

Fig. 15. In (a) outlined in red is Central sector studied in more details. The star indicates the location of the PSs selected to show in (b) the related time series. (b) Vertical displacement time-series and corresponding linear rates of subsidence. ERS (green) and Envisat (blue) time series are shown.

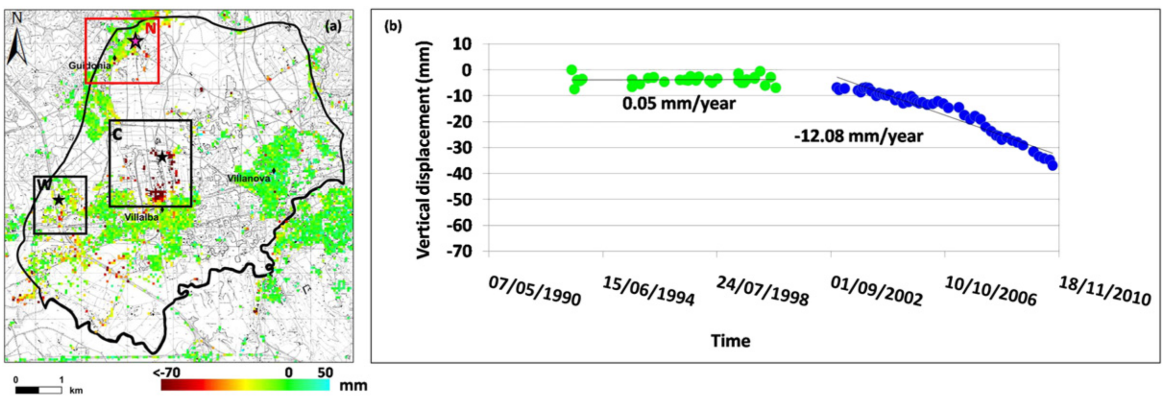

Fig. 16. In (a) outlined in red is Northern sector studied in more details. The star indicates the location of the PSs selected to show in (b) the related time series. (b) Vertical displacement time-series and corresponding linear rates of subsidence. ERS (green) and Envisat (blue) time series are shown.

4. Discussion

The results of the A-DInSAR analyses have been interpreted by accounting for the local geological features and the spatial and temporal piezometric evolution over time to attain a comprehensive interpretation of the subsidence process and to derive more insight into the triggering factors.

As discussed above, the piezometric surface has been effectively modelled from 1954 to 2008, thus highlighting the effects induced by pumping over time. Specifically, the underground water cone caused by the quarry activities gradually deepens and affects a wider portion of the plain (Fig. 18), ranging from −3 m of drawdown in 1969 to −8 m in 1992 in the open pit area. Then, beginning in 1998, when the extraction of water reached approximately 1.5 m^3/s, the water table

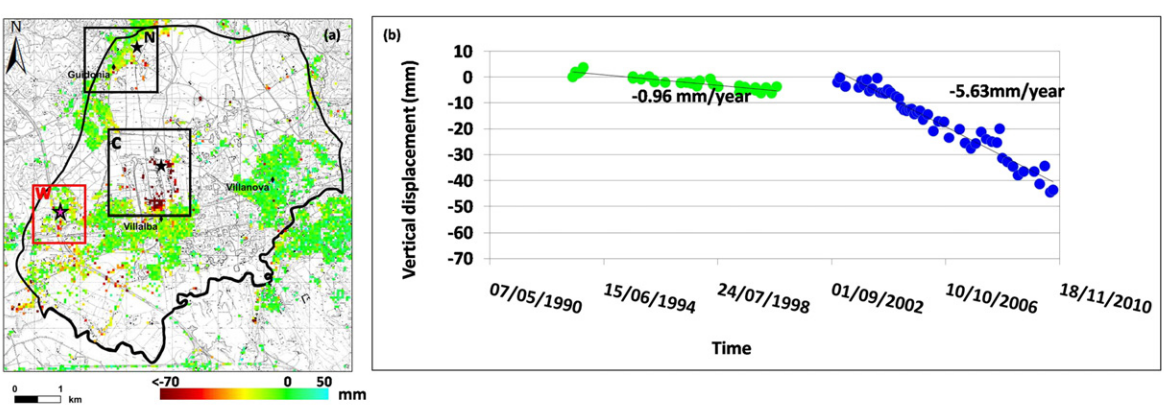

Fig. 17. In (a) outlined in red is Western sector studied in more details. The star indicates the location of the PSs selected to show in (b) the related time series. (b) Vertical displacement time-series and corresponding linear rates of subsidence. ERS (green) and Envisat (blue) time series are shown.

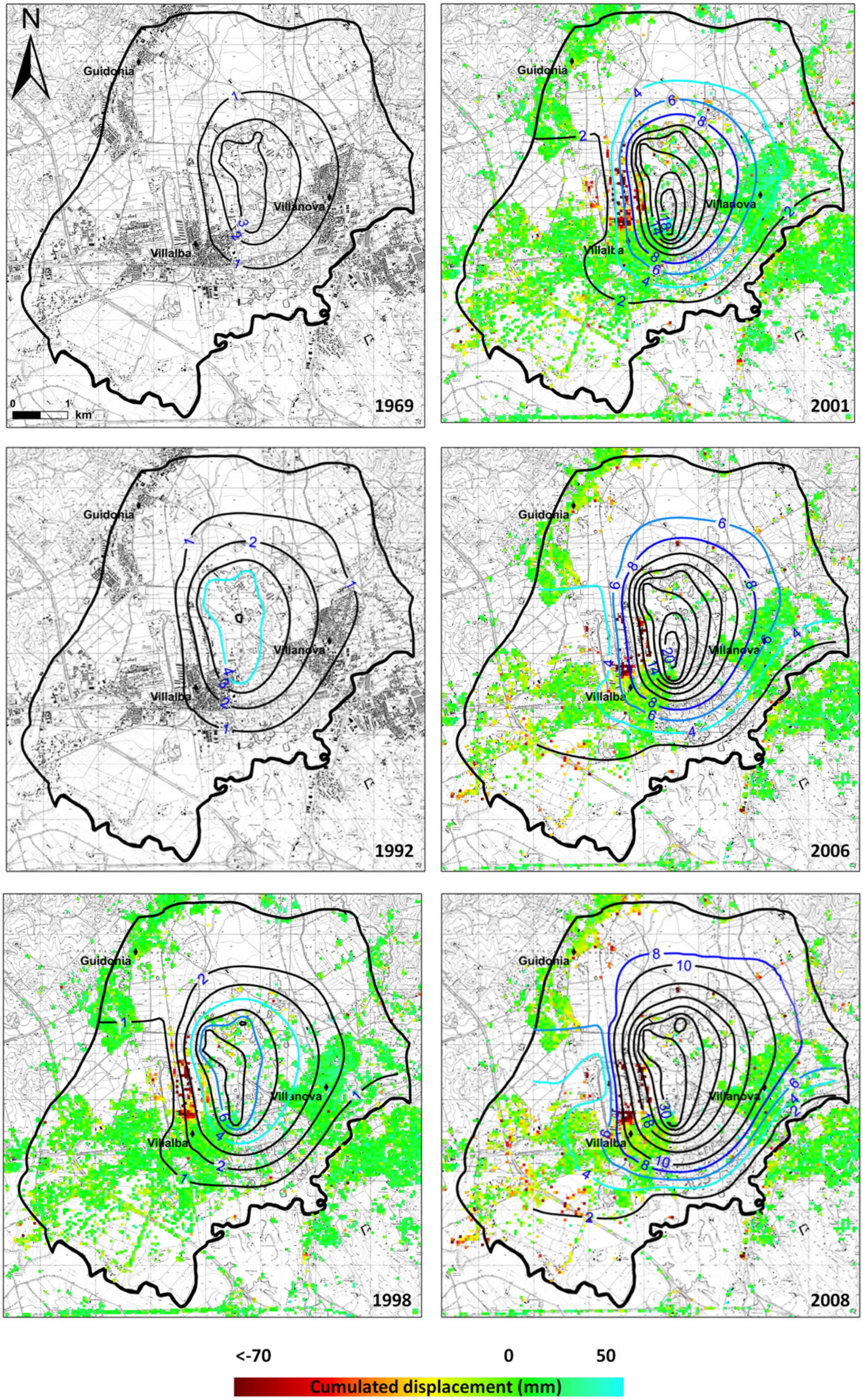
N
Guidonia
Villanova
Villalba
0 1 km
1969
2001
1992
2006
1998
2008
<-70
0
50
Cumulated displacement (mm)

underwent a sharp decrease, reaching −18 m in 2001. In 2008, when the extracted water was approximately 4 m^3/s, the water table reached a depth of 32 m b.g.l. Furthermore, the dewatering cone has extended over years, thus affecting portions of the plain farther away from the main quarry area.

The Central sector is affected by the decrease in the water table by 4 m in 1998. In 2008, the simulated drop reaches 10 m.

The simulated piezometric surface in the Northern sector underwent a decrease of less than 1 m in 1992. In 1998, the decrease was between 1 m and 2 m; in 2001, it reached 4 m. In 2006, the drop was between 4 m and 6 m. At the end of 2008, the decrease was between 6 m and 8 m. (Fig. 18).

In the Western sector, the decrease was less than 2 m until 2001, and it reached 4 m at the end of 2008.

The overall mechanism linking the piezometric surface variations and the detected subsidence phenomenon in time is thus explained: when water is pumped from the travertine aquifer, whose piezometric level roughly coincided with the ground level under undisturbed conditions, a gradient is created, thus causing a water pressure reduction in the compressible soils on top of the travertine bedrock. As a result of the water pressure decrease in the compressive soil pores, these soils experienced a consolidation process.

The A-DInSAR deformation data showed a good relationship with the simulated piezometric level changes, thus allowing for the identification of different patterns of ground surface behaviour in the study area.

Specifically, the ground deformations that occurred between 1993 and 2001 were localised in the areas affected by the cone of depression caused by the pumping activities in the quarry areas. However, although the areas with travertine outcrops showed minimal or null deformation, the areas characterised by the presence of compressible deposits showed vertical deformations proportional to the variations in piezometric level (Central sector). Furthermore, the areas characterised by compressible deposits, where the decrease in the piezometric level did not occur, did not experience detectable deformations (Northern sector and Western sector) (Fig. 18).

The same linear relationship between the decrease in the piezometric levels and the vertical deformations is confirmed in 2003–2010. In this period, the cone of depression had expanded and deepened in time and in space, affecting the entire basin, and the PS data clearly show the appearance of new areas of subsidence (Fig. 18). The areas newly affected by subsidence are located where the thickness of the compressible materials is greater (Northern sector and Western sector). In addition, in this case, the interferometric data returned negligible LOS displacements in areas where the travertine locally outcrops.

Hence, the full-site A-DInSAR analyses were able to define the overall subsidence mechanism occurred in the Acque Albule plain: local geological conditions control the magnitude of the process, whereas its timing is driven by hydrogeological variations in time.

Moreover, the full-site A-DInSAR results represented a starting point for performing local-scale interferometric analyses. In particular, our objective was to deepen the understanding of subsidence trigger timing. As we observed in Section 3.2, some sectors localised in the marginal areas of the Acque Albule Basin experienced the beginning of the subsidence process during the Envisat observation period. The main concept was to observe the evolution in time and space of the detected ground deformation with a more accurate time series of the displacements to better identify the triggering time within the Envisat observation period. As stated above (Section 3.1.2), the absence of APS estimation and, furthermore, the displacement estimation performed also using a 'no-model' approach (applied in these specific analyses), allowed for an increase in the reliability of the thus-attained time series because the time series are not influenced by any linear model, as was true in the full-site analyses.

The results of the local-scale processing of the Envisat data are summarised in Fig. 19. The time series characterised by non-linear behaviour clearly demonstrate how the process of subsidence expands over the plain. For the areas to the north and west, it was possible to understand when the process started. The time series of the Northern and Western sectors show two linear deformation trends with different velocities. In particular, the subsidence process is activated beginning at certain point in the displacement time series. For the Northern sector, it is possible to characterise three different trends in the deformation rate in the PS time series. In particular, from the observation of the time series in Fig. 19a, no deformations could be detected up through 2004, whereas in 2004–2007, the cumulated displacements reached approximately 20 mm (i.e., 5 mm/y). From 2007 to 2010, a maximum deformation of 80 mm was reached.

Comparing these results with the variations in the water table, the decrease in the groundwater level in this area was less than 2 m until 2001, and it was between 4 m and 6 m in 2007. Finally, in late 2008, the drawdown was over 6 m. Therefore, the activation time of the subsidence in the Northern sectors is strictly related to the involvement in the cone of depression, whereas the magnitude of the process is governed by the local stratigraphy. This evidence is supported by the behaviour of some PSs farther from the pumping "epicentre" that experienced smaller vertical displacements than other points located closer. The associated stratigraphy reveals a thicker layer of compressible soils at the more distant points than at the closer points. We observed that the changeover between the areas with subsidence (orange to yellow colours in Fig. 19) and areas without subsidence (green colours) occurred in a narrow zone, less than 1 km wide. The geologic data show that this area corresponds to the transition zone between the compressible deposits and volcanic and sedimentary bedrock.

A similar result was obtained for the Western sector, where we observed an acceleration of the process since 2008 (Fig. 19b). The relationship between the geological setting and the hydrogeological variations is also here confirmed; in this case, even with a greater thickness of compressible deposits in the centre of the sector, the total vertical displacement is less because the decrease in the water table reached only 2–4 m in this area.

To better constrain the relationship between the subsidence and the thickness of the compressible sediments, we assigned to the 97 available boreholes and, thus, to the related stratigraphic log the vertical cumulative displacement value measured for 1992–2008 in the closest PS, imposing a maximum reliable distance of 100 m. Such a limit of distance was assumed as representative considering the lateral heterogeneity of the distribution of the deposits.

As a result, 20% of the boreholes had no available PSs sufficiently close for a significant comparison. A vertical cumulative displacement was instead assigned to the remaining 80% of boreholes, i.e. 78. Furthermore, also a value of groundwater drawdown was associated to each borehole by considering its location with respect to the simulated evolution of the piezometric surface (Fig. 18).

The so obtained dataset allowed us to perform a comparative analysis of the relationships between the thickness of compressible soils, the cumulative vertical displacement and the amount of groundwater drawdown associated to each borehole. Such an analysis allowed us to highlight some significant correlation, especially in terms of combined "critical" thresholds: the cumulative vertical displacement does not exceed 4 cm if the thickness of compressible deposits is less than 6 m and the drawdown less than 4 m, while higher vertical displacements occur

Fig. 18. Evolution of the cone of depression induced by pumping overlaid on cumulated deformation maps for different time steps. In order to better observe the expansion of the underground water cone and the local lowering of the water table, the isolines representing 4, 6 and 8 m are marked with different tones of blue.

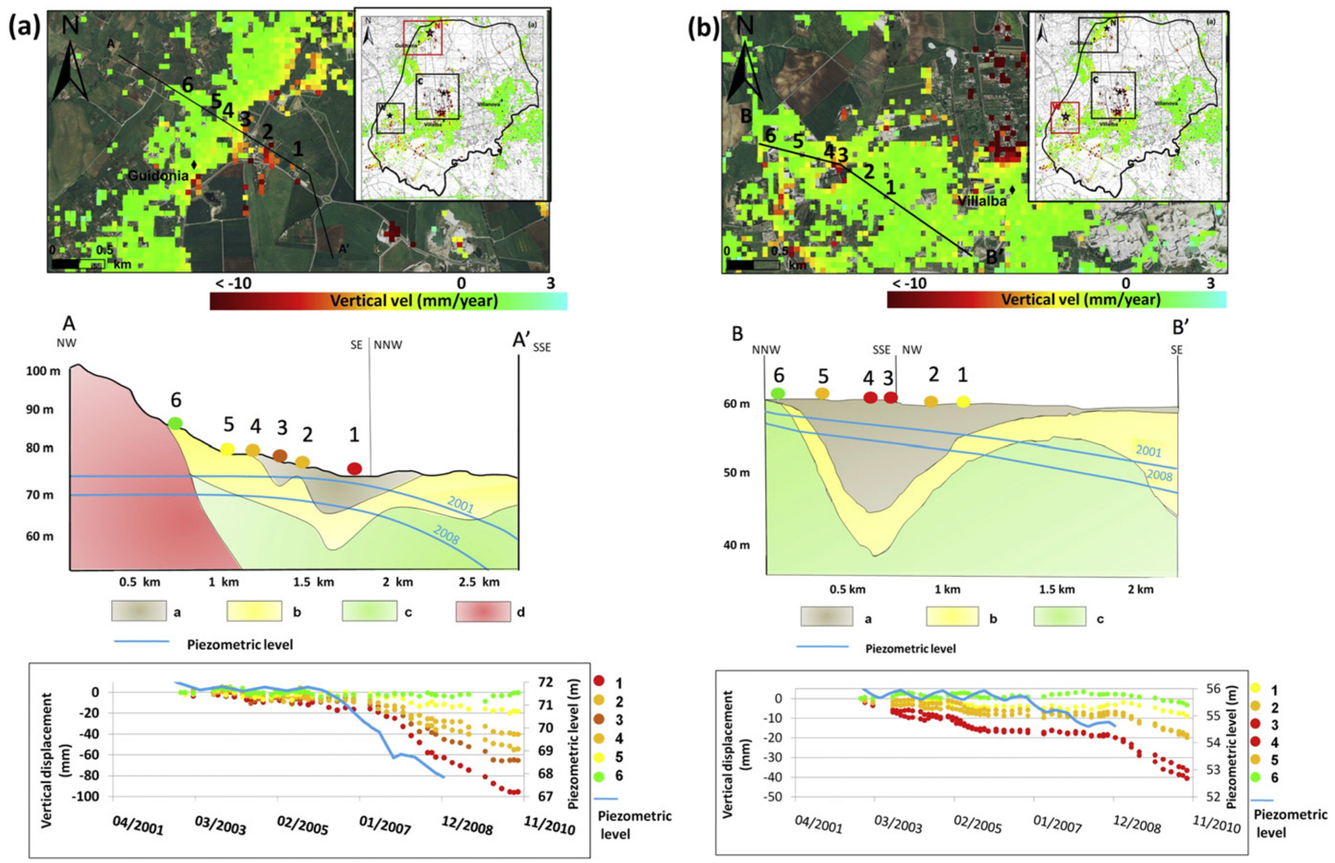

Fig. 19. Local-scale results of Northern (a) and Western (b) sectors. We reported the geological sketches (with a strong vertical exaggeration) associated to the selected PSs as well as their location. Charts showing the relationships between the time histories of modelled dewatering and vertical displacement of selected PSs along sections. Key to legend: a) Organic clays and peats; b) Loose travertine; c) Travertine; d) Volcanic and sedimentary bedrock. Vertical scales are different to appreciate different piezometric variations in the two sites.

if the thresholds of 6 m and 4 m are exceeded by compressive soil thickness and groundwater drawdown, respectively. These results are shown and summarised in Fig. 20.

It is worth noting that this analysis does not include the construction quality of the buildings, the typology of the foundations and the soil–foundation interactions, although in the A-DInSAR analysis, structures themselves very often represent the targets that the backscatter phase signals related to the deformation measurements. Furthermore, the compressible soil thickness and the groundwater drawdown being equal, a slight variability of vertical displacements can sometimes be observed: such an effect can derive by a difference in terms of arrival time of the depression cone and, thus, in terms of consolidation phase.

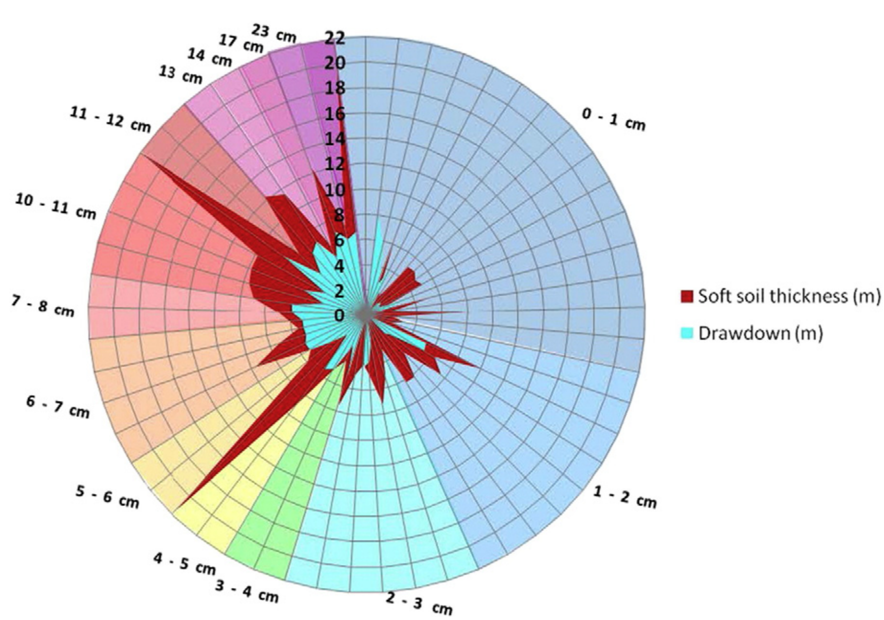

Fig. 20. The graph shows for each borehole (which corresponds to a radius) data of the thickness of the compressible deposits and drawdown (expressed in metres, vertical scale bar) and vertical cumulated displacement (expressed in centimetres, along circumference).

5. Conclusions

Using the combination of geological and geotechnical data with hydrogeological modelling calibrated on piezometric data-set, we were able to explain the spatial and temporal evolution of a subsidence process related to the huge groundwater drawdown experienced in the last decades in a recently anthropogenically stressed area.

The subsidence process has been thoroughly quantified in the time interval 1993–2010 by satellite A-DInSAR analyses performed on four different datasets acquired in double orbital geometries.

The investigations carried out confirm both the overall process on a wide scale and the local behaviours analysed in detail using ad hoc interferometric analyses, combined with local engineering–geological stratigraphic conditions.

The specific role of the main controlling factors has been well constrained by the here performed diagnosis of the already occurred subsidence process: the groundwater level variations drive the timing of subsidence triggering over the area, whereas the local geological conditions – i.e. the thickness of the compressible deposits overlaying the travertine in its turn hosting the exploited aquifer – drive the magnitude of the deformation process.

The back-analysis case history here discussed encourages the research towards the forecasting of the on-going evolution of the subsidence process caused by groundwater exploitation in geologically well-known areas. Systems mainly based on the continuous monitoring of the groundwater levels by means of a network of piezometers distributed in the area could be able to anticipate either the onset or the acceleration phases of the subsidence. We thrust that the coupling of such a type of monitoring network with sporadic satellite and ad-hoc planned A-DInSAR analyses could be a very efficient self-controlling monitoring platform.

Acknowledgments

The present work is within the framework of a research project (PRIN 2009 — "Analysis, monitoring and control of geological instability interacting with human activities") funded by the Italian Ministry of Education, University and Research (MIUR) (PRIN 2009 - 2009PB8HER_001), Principal Investigator: Francesca Bozzano. SAR data have been provided by the European Space Agency, in the frame of the Cat-1 project "Geological reconstruction and monitoring in recently urbanised areas affected by subsidence" (Id 13097). The authors would also like to thank students Elio Brunetti, Valentina Carucci, Luigi Rosella and Chiara Sbarbati for their support in the field activities.

References

Amelung, F., Galloway, D. L., Bell, J. W., Zebker, H. A., & Laczniak, R. J. (1999). Sensing the ups and downs of Las Vegas: InSAR reveals structural control of land subsidence and aquifer-system deformation. *Geology*, *27*(6), 483–486.

Berardino, P., Fornaro, G., Lanari, R., & Sansosti, E. (2002). A new algorithm for surface deformation monitoring based on small baseline differential SAR interferograms. *IEEE transactions on geoscience and remote sensing*, *40*, 2375–2383.

Billi, A., Valle, A., Brilli, M., Faccenna, C., & Funiciello, R. (2007). Fracture-controlled fluid circulation and dissolutional weathering in sinkhole-prone carbonate rocks from central Italy. *Journal of structural geology*, *29*(3), 385–395.

Bock, Y., Wdowinski, S., Ferretti, A., Novali, F., & Fumagalli, A. (2012). Recent subsidence of the Venice Lagoon from continuous GPS and interferometric synthetic aperture radar. *Geochemistry, geophysics, geosystems*, *13*(3). http://dx.doi.org/10.1029/2011GC003976.

Boni, C., Bono, P., & Capelli, G. (1986). Schema idrogeologico dell'Italia Centrale. *Memorie della Societa Geologica Italiana*, *35*, 991–1012.

Bono, P. (2005). *Indagini idrogeologiche per determinare le cause dei dissesti agli edifici di via Cesare Augusto e aree limitrofe, in località Bagni di Tivoli. Dip. Scienze della Terra (Università La Sapienza, Roma) – Regione Lazio.* (in Italian).

Bru, G., Herrera, G., Tomás, R., Duro, J., De la Vega, R., & Mulas, J. (2013). Control of deformation of buildings affected by subsidence using persistent scatterer interferometry. *Structure and infrastructure engineering*, *9*(2), 188–200.

Brunetti, E., Jones, J. P., Petitta, M., & Rudolph, D. L. (2013). Assessing the impact of large-scale dewatering on fault-controlled aquifer systems: A case study in the Acque Albule basin (Tivoli, central Italy). *Hydrogeology journal*, *21*(2), 401–423.

Budhu, M., & Adiyaman, I. B. (2010). Mechanics of land subsidence due to groundwater pumping. *International journal for numerical and analytical methods in geomechanics*, *34*(14), 1459–1478.

Burbey, T. (2002). The influence of faults in basin-fill deposits on land subsidence, Las Vegas Valley, Nevada, USA. *Hydrogeology journal*, *10*(5), 525–538. http://dx.doi.org/10.1007/s10040-002-0215-7.

Bürgmann, R., Rosen, P. A., & Fielding, E. J. (2000). Synthetic aperture radar interferometry to measure Earth's surface topography and its deformation. *Annual review of earth and planetary sciences*, *28*(1), 169–209.

Cabral-Cano, E., Dixon, T. H., Miralles-Wilhelm, F., Díaz-Molina, O., Sánchez-Zamora, O., & Carande, R. E. (2008). Space geodetic imaging of rapid ground subsidence in Mexico City. *Geological Society of America bulletin*, *120*(11–12), 1556–1566.

Capelli, G., Cosentino, D., Messina, P., Raffi, R., & Ventura, G. (1987). Modalità di ricarica e assetto strutturale dell'acquifero delle sorgenti Capore–S. Angelo (Monti Lucretili–Sabina Meridionale) (recharge and structural setting of the Capore-S. Angelosprings' reservoir–Lucretili Mt. s-South Sabina). *Geologica romana*, *26*, 419–447 (in Italian).

Capelli, G., & Mazza, R. (2006). *Indagini geologiche, strutturali, stratigrafiche e idrogeologiche nell'area di Tivoli Terme (RM) e Villalba di Guidonia (RM).* Convenzione di ricerca, Relazione finale. Università degli studi di Roma TRE. Gruppo di lavoro di idrogeologia. Inedito (in Italian).

Capelli, G., Mazza, R., & Gazzetti, C. (2005). *Strumenti e strategie per la tutela e l'uso compatibile della risorsa idrica nel Lazio. Gli acquiferi vulcanici. Quaderni di Tecniche di Protezione Ambientale*, *78*, (in Italian).

Capelli, G., Mazza, R., & Taviani, S. (2005). *Studi idrogeologici per la definizione degli strumenti operativi del piano stralcio per l'uso compatibile delle risorse idriche sotterranee nell'ambito dei sistemi acquiferi prospicienti i territori vulcanici laziali.* Relazione inedita, 132 Università degli Studi di Roma III, dipartimento di Scienze Geologiche, laboratorio di Idrogeologia (in Italian).

Carucci, V., Petitta, M., & Aravena, R. (2012). Interaction between shallow and deep aquifers in the Tivoli Plain (Central Italy) enhanced by groundwater extraction: a multi-isotope approach and geochemical modeling. *Applied geochemistry*, *27*(1), 266–280.

Chaussard, E., Amelung, F., Abidin, H., & Hong, S. H. (2013). Sinking cities in Indonesia: ALOS PALSAR detects rapid subsidence due to groundwater and gas extraction. *Remote sensing of environment*, *128*, 150–161.

Chaussard, E., Wdowinski, S., Cabral-Cano, E., & Amelung, F. (2014). Land subsidence in central Mexico detected by ALOS InSAR time-series. *Remote sensing of environment*, *140*, 94–106.

Colombo, D., Farina, P., Moretti, S., Nico, G., & Prati, C. (2003). *Land subsidence in the Firenze–Prato–Pistoia basin measured by means of spaceborne SAR interferometry, Geoscience and Remote Sensing Symposium, 2003.* IGARSS'03. Proceedings. 2003 IEEE International.

Damoah-Afari, P., Ding, X., Lu, Z., & Li, Z. W. (2008). *Detection ground settlement of Shanghai using interferometric synthetic radar (InSAR) techniques. The International Archives of the Photogrammetry, Remote Sensing and Spatial Information Sciences*, *37*. (pp. 117–124) (Part B7).

Dixon, T. H., Amelung, F., Ferretti, A., Novali, F., Rocca, F., Dokka, R., et al. (2006). Space geodesy: Subsidence and flooding in New Orleans. *Nature*, *441*(7093), 587–588. http://dx.doi.org/10.1038/441587a.

Dragoni, W. (1998). Some considerations on climatic changes, water resources and water needs in the Italian region south of 43 N. In A. Issar, & N. Brown (Eds.), *Water, environment and society in times of climatic change* (pp. 241–271). Dordrecht, The Netherlands: Kluwer.

Faccenna, C. (1994). Structural and hydrogeological features of Pleistocene shear zones in the area of Rome (central Italy). *Annali di Geofisica*, *37*(1), 121–133.

Faccenna, C., Funiciello, R., & Mattei, M. (1994). Late Pleistocene N–S shear zones along the Latium Tyrrhenian margin: structural characters and volcanological implications. *Bollettino di Geofisica Teorica ed Applicata*, *36*(141–144), 507–522.

Faccenna, C., Soligo, M., Billi, A., De Filippis, L., Funiciello, R., Rossetti, C., et al. (2008). Late Pleistocene depositional cycles of the Lapis Tiburtinus travertine (Tivoli, Central Italy): Possible influence of climate and fault activity. *Global and planetary change*, *63*(4), 299–308.

Ferretti, A., Fumagalli, A., Novali, F., Prati, C., Rocca, F., & Rucci, A. (2011). A new algorithm for processing interferometric data-stacks: SqueeSAR. *IEEE transactions on geoscience and remote sensing*, *49*(9), 3460–3470.

Ferretti, A., Prati, C., & Rocca, F. (2000). Nonlinear subsidence rate estimation using permanent scatterers in differential SAR interferometry. *IEEE transactions on geoscience and remote sensing*, *38*(5), 2202–2212. http://dx.doi.org/10.1109/36.868878.

Ferretti, A., Prati, C., & Rocca, F. (2001). Permanent scatterers in SAR interferometry. *IEEE transactions on geoscience and remote sensing*, *39*(1), 8–20.

Floris, M., Bozzano, F., Strappaveccia, C., Baiocchi, V., & Prestininzi, A. (2014). Qualitative and quantitative evaluation of the influence of anthropic pressure on subsidence in a sedimentary basin near Rome. *Environmental earth sciences*. http://dx.doi.org/10.1007/s12665-014-3317-3.

Fruneau, B., & Sarti, F. (2000). Detection of ground subsidence in the city of Paris using radar interferometry: Isolation of deformation from atmospheric artifacts using correlation. *Geophysical Research Letters*, *27*, 3981–3984.

Funiciello, R., Faccenna, C., De Filippis, L., & Rossetti, C. (2005). *Indagini per determinare le cause dei dissesti agli edifici di Via Cesare Augusto, e aree limitrofe, in località Bagni di Tivoli: Assetto strutturale e Microzonazione sismica. Rep. Cron. N.3561 del 17.01.05.* (in Italian).

Gabriel, A., Goldstein, R., & Zebker, H. A. (1989). Mapping small elevation changes over large areas — Differential radar interferometry. *Journal of geophysical research-solid earth and planets*, *94*, 9183–9191.

Guéguen, Y., Deffontaines, B., Fruneau, B., Al Heib, M., De Michele, M., Raucoules, D., et al. (2009). Monitoring residual mining subsidence of Nord/Pas-de-Calais coal basin from differential and Persistent Scatterer Interferometry (Northern France). *Journal of applied geophysics*, *69*(1), 24–34.

Hanssen, R. F. (2005). Satellite radar interferometry for deformation monitoring: A priori assessment of feasibility and accuracy. *International journal of applied earth observation and geoinformation*, *6*(3), 253–260.

Harbaugh, A. W. (2005). *MODFLOW-2005, the US Geological Survey modular ground-water model: The ground-water flow process* (pp. 6-A16). US Department of the Interior, US Geological Survey.

Heleno, S. I., Oliveira, L. G., Henriques, M. J., Falcão, A. P., Lima, J. N., Cooksley, G., et al. (2011). Persistent Scatterers Interferometry detects and measures ground subsidence in Lisbon. *Remote sensing of environment*, *115*(8), 2152–2167.

Hoffmann, J., Zebker, H. A., Galloway, D. L., & Amelung, F. (2001). Seasonal subsidence and rebound in Las Vegas Valley, Nevada, observed by synthetic aperture radar interferometry. *Water resources research*, *37*(6), 1551–1566.

Hooper, A., Zebker, H., Segall, P., & Kampes, B. (2004). A new method for measuring deformation on volcanoes and other natural terrains using InSAR persistent scatterers. *Geophysical research letters*, *31*(23), L23611. http://dx.doi.org/10.1029/2004GL021737.

Hung, W. C., Hwang, C., Chen, Y. A., Chang, C. P., Yen, J. Y., Hooper, A., et al. (2011). Surface deformation from persistent scatterers SAR interferometry and fusion with leveling data: A case study over the Choushui River Alluvial Fan, Taiwan. *Remote sensing of environment*, *115*(4), 957–967.

Jung, H. C., Kim, S. W., Jung, H. S., Min, K. D., & Won, J. S. (2007). Satellite observation of coal mining subsidence by persistent scatterer analysis. *Engineering geology*, *92*, 1–13.

Kampes, B. M. (2006). *Radar interferometry persistent scatterers technique.* Dordrecht, The Netherlands: Springer.

La Vigna, F., Mazza, R., & Capelli, G. (2013). Detecting the flow relationships between deep and shallow aquifers in an exploited groundwater system, using long-term monitoring data and quantitative hydrogeology: the Acque Albule basin case (Rome, Italy). *Hydrological Processes*, *27*(22), 3159–3173.

Lombardi, L. (2005). *Indagini geochimiche per determinare le cause dei dissesti agli edifici di Via Cesare Augusto ed aree limitrofe, in località Bagni di Tivoli.* Analisi di campioni di acqua e gas. Contratto di ricerca Regione Lazio n. 5350 del 11/01/2005 (in Italian).

Lu, Z., Masterlark, T., Power, J., Dzurisin, D., & Wicks, C. (2002). Subsidence at Kiska volcano, western Aleutians, detected by satellite radar interferometry. *Geophysical research letters*, *29*(18). http://dx.doi.org/10.1029/2002GL014948 (2-1-2-4).

Massonnet, D., Briole, P., & Arnaud, A. (1995). Deflation of Mount Etna monitored by spaceborne radar interferometry. *Nature*, *375*(6532), 567–570.

Massonnet, D., Feigl, K., Rossi, M., & Adragna, F. (1994). Radar interferometric mapping of deformation in the year after the Landers earthquake. *Nature*, *369*(6477), 227–230.

Massonnet, D., Rossi, M., Carmona, C., Adragna, F., Peltzer, G., Feigl, K., et al. (1993). The displacement field of the Landers earthquake mapped by radar interferometry. *Nature*, *364*(6433), 138–142.

Maxia, C. (1950). *Il Bacino delle Acque Albule (Lazio).* Contributi di Scienze Geologiche, Supp. Ric. SC. 20–27, Univ. Roma (in Italian).

Meckel, T. A., ten Brink, U. S., & Williams, S. J. (2006). Current subsidence rates due to compaction of Holocene sediments in southern Louisiana. *Geophysical research letters*, *33*, L11403. http://dx.doi.org/10.1029/2006GL026300.

Modoni, G., Darini, G., Spacagna, R. L., Saroli, M., Russo, G., & Croce, P. (2013). Spatial analysis of land subsidence induced by groundwater withdrawal. *Engineering geology*, *167*, 59–71.

Osmanoğlu, B., Dixon, T. H., Wdowinski, S., Cabral-Cano, E., & Jiang, Y. (2011). Mexico City subsidence observed with persistent scatterer InSAR. *International journal of applied earth observation and geoinformation*, *13*(1), 1–12.

Perissin, D., & Wang, T. (2012). Repeat-pass SAR interferometry with partially coherent targets. *IEEE transactions on geoscience and remote sensing*, *50*(1), 271–280.

Perissin, D., Wang, Z., & Wang, T. (2011). *The SARPROZ InSAR tool for urban subsidence/manmade structure stability monitoring in China.* Proc. of ISRSE 2010, Sidney, Australia, 10–15 April 2011.

Petitta, M., & Del Bon, A. (2003). *Indagini idrogeologiche sulle Sorgenti delle Acque Albule (Bagni di Tivoli).* Università 'La Sapienza' Roma. Reserved document (In Italian).

Petitta, M., Primavera, P., Tuccimei, P., & Aravena, R. (2011). Interaction between deep and shallow groundwater systems in areas affected by Quaternary tectonics (Central Italy): a geochemical and isotope approach. *Environmental earth sciences*, *63*(1), 11–30.

Phien-wej, N., Giao, P. H., & Nutalaya, P. (2006). Land subsidence in Bangkok, Thailand. *Engineering geology*, *82*, 187–201.

Prestininzi, A. (2008). *Relazione conclusiva relativa alle convenzioni stipulate tra il Centro di Ricerca CE.RI. e la Regione Lazio (30/01/2006 e successiva del 04/07/2006), inerente agli studi e alle indagini condotte nelle zone soggette a fenomeni di subsidenza di Tivoli-Guidonia.* CERI La Sapienza — Regione Lazio Protezione Civile (in Italian).

Raspini, F., Loupasakis, C., Rozos, D., & Moretti, S. (2013). Advanced interpretation of land subsidence by validating multi-interferometric SAR data: the case study of the Anthemountas basin (Northern Greece). *Natural hazards and earth system sciences*, *13*, 2425–2440. http://dx.doi.org/10.5194/nhess-13-2425-2013.

Raucoules, D., Bourgine, B., De Michele, M., Le Cozannet, G., Closset, L., Bremmer, C., et al. (2009). Validation and intercomparison of Persistent Scatterers Interferometry: PSIC4 project results. *Journal of applied geophysics*, *68*(3), 335–347.

Raucoules, D., Colesanti, C., & Carnec, C. (2007). Use of SAR interferometry for detecting and assessing ground subsidence. *Comptes rendus geoscience*, *339*(5), 289–302.

Raucoules, D., Le Mouélic, S., Carnec, C., Maisons, C., & King, C. (2003). Urban subsidence in the city of Prato (Italy) monitored by satellite radar interferometry. *International journal of remote sensing*, *24*(4), 891–897.

Salvi, S., Pirro, M., Gasparini, C., Stramondo, S., Pagliuca, M. N., Atzori, S., et al. (2004). Le deformazioni del suolo ricavate da dati satellitari in un settore a rischio sinkhole del Bacino delle Acque Albule (Lazio). *1° Convegno APAT, Roma, 20–21 Maggio* (pp. 623–632) (in Italian).

Samsonov, S., d'Oreye, N., & Smets, B. (2013). Ground deformation associated with post-mining activity at the French–German border revealed by novel InSAR time series method. *International journal of applied earth observation and geoinformation*, *23*, 142–154.

Teatini, P., Castelletto, N., Ferronato, M., Gambolati, G., Janna, C., Cairo, E., et al. (2011). Geomechanical response to seasonal gas storage in depleted reservoirs: A case study in the Po River basin, Italy. *Journal of geophysical research, earth surface*, *116*, F02002. http://dx.doi.org/10.1029/2010JF001793.

Tesauro, M., Berardino, P., Lanari, R., Sansosti, E., Fornaro, G., & Franceschetti, G. (2000). Urban subsidence inside the city of Napoli (Italy) observed by satellite radar interferometry. *Geophysical research letters*, *27*(13), 1961–1964.

Tomás, R., Herrera, G., Delgado, J., Lopez-Sanchez, J. M., Mallorquí, J. J., & Mulas, J. (2010). A ground subsidence study based on DInSAR data: calibration of soil parameters and subsidence prediction in Murcia City (Spain). *Engineering geology*, *111*(1), 19–30.

Waterloo Hydrogeologic Inc. (2006). *Visual MODFLOW user's manual.* Ontario: Waterloo Hydrogeologic Inc.

Xue, Y. Q., Zhang, Y., Ye, S. J., Wu, J. C., & Li, Q. F. (2005). Land subsidence in China. *Environmental geology*, *48*(6), 713–720.